

All-Dielectric Toroidal Metasurfaces for Angular-Dependent Resonant Polarization Beam Splitting

Dimitrios C. Zografopoulos, José Francisco Algorri, Walter Fuscaldo, José Miguel López-Higuera, Ricardo Vergaz, José Manuel Sánchez-Pena, Ion-Anastasios Karolos, Romeo Beccherelli, Vassilios E. Tsioukas, Traianos V. Yioultsis, and Emmanouil E. Kriezis*

An all-dielectric metasurface exhibiting a strong toroidal resonance is theoretically designed and experimentally demonstrated as an angular-dependent resonant polarization beam-splitter in the microwave K-band. The metasurface is fabricated by embedding a square periodic array of high-permittivity ceramic cuboid resonators in a 3D-printed substrate of polylactic acid. It is demonstrated that by properly selecting the resonator geometry and by tuning the angle of incidence through mechanical rotation, the metasurface can switch between a polarization beam splitting and bandpass or bandstop operation. Such performance is achieved by exploiting the highly asymmetric Fano spectral profile of the toroidal resonance and the very low (high) dispersion of the associated p-(s-) polarized mode resulting from the resonant toroidal dipole mode's field profile, as evidenced by both full-wave and band structure simulations. Theoretically infinite extinction ratios are achievable for polarization beam splitting operation with very low insertion losses and adjustable bandwidth. The experimental demonstration of such a compact, all-dielectric metasurface expands the research portfolio of resonant metasurfaces toward not only the investigation of the intriguing physics of toroidal modes but also to the engineering of functional millimeter-wave components for polarization control, for instance, in the context of 5G wireless communication networks.

1. Introduction

Metasurfaces (MS) are electromagnetically thin artificial media composed of resonant scatterers, metallic, or dielectric, in an array configuration with subwavelength periodicity.^[1–3] The collective oscillations of the resonant MS atoms enable the control of the wavefront, intensity, polarization, or spectrum of propagating electromagnetic (EM) waves in unprecedented ways, thus eliminating the need for bulky components. A subset of MS that has been attracting growing scientific and technological attention is all-dielectric MS, thanks to their rich potential for EM wave manipulation without the drawback of ohmic losses, which are intrinsic to their metallic/plasmonic counterparts.^[4]

In particular, all-dielectric MS composed of high-permittivity scatterers that support a plethora of Mie resonances have been demonstrated as a promising platform for compact, low-loss components in a multitude of applications among

Dr. D. C. Zografopoulos, Dr. W. Fuscaldo, Dr. R. Beccherelli
Consiglio Nazionale delle Ricerche
Istituto per la Microelettronica e Microsistemi
Via del fosso del cavaliere 100, Rome 00133, Italy
E-mail: dimitrios.zografopoulos@artov.imm.cnr.it

Dr. J. F. Algorri, Prof. J. M. López-Higuera
Photonics Engineering Group
University of Cantabria
Santander 39005, Spain

 The ORCID identification number(s) for the author(s) of this article can be found under <https://doi.org/10.1002/adom.202002143>.

© 2021 The Authors. Advanced Optical Materials published by Wiley-VCH GmbH. This is an open access article under the terms of the Creative Commons Attribution-NonCommercial License, which permits use, distribution and reproduction in any medium, provided the original work is properly cited and is not used for commercial purposes.

DOI: 10.1002/adom.202002143

Prof. J. M. López-Higuera
CIBER-bbn
Instituto de Salud Carlos III
Madrid 28029, Spain

Prof. J. M. López-Higuera
Instituto de Investigación Sanitaria Valdecilla (IDIVAL)
Santander 39011, Spain

Prof. R. Vergaz, Prof. J. M. Sánchez-Pena
Department of Electronic Technology
Carlos III University of Madrid
Madrid 28911, Spain

I.-A. Karolos, Prof. V. E. Tsioukas
School of Rural and Surveying Engineering
Aristotle University of Thessaloniki
Thessaloniki 54124, Greece

Prof. T. V. Yioultsis, Prof. E. E. Kriezis
School of Electrical and Computer Engineering
Aristotle University of Thessaloniki
Thessaloniki 54124, Greece

which lensing,^[5] reflection control and wavefront shaping,^[6–8] manipulation of light emission or photoluminescence,^[9–11] polarimetry,^[12] highly-selective filtering,^[13,14] or enhancement of nonlinear processes.^[15,16] In this regard, it is common to study their resonant properties in terms of electric and magnetic multipoles, which are derived from the Taylor expansion of their EM fields and potentials, in order to gain physical insight into the possibility for intense light-matter interaction. Furthermore, by decomposition of the moment tensor, a third class of EM modes can be identified, the toroidal multipoles. The archetypal structure that generates a toroidal (dipole) moment is that of a solenoid bent into a torus: the poloidal current flowing through the solenoid generates a magnetic field inside the torus, whereas the resulting toroidal moment is parallel to the axis of revolution of the torus.^[17]

Toroidal modes have been long known in physics, for instance, to describe parity violations and weak interactions in atomic nuclei,^[18] as models for stable atoms^[19] or even dark matter.^[20] However, even though toroidal multipoles do manifest in natural media,^[21] their EM response is usually very weak and difficult to measure as it is screened by the much stronger electric and magnetic multipoles. This can be overcome in specially engineered metasurfaces, where toroidal resonances become dominant, thus enabling not only the investigation of their elusive physics^[22–24] but also their use in various applications.^[25–28] As a result, the growing research efforts put in the study of toroidal MS have led to numerous demonstrations of their practical potential, for example, for polarization conversion,^[29] beam steering,^[30] high-quality factor filtering,^[23,31–35] and narrowband absorption and directional emission.^[36]

Although several of the thus far investigated toroidal MS employ metallic meta-atoms,^[31,37–39] in certain cases these have an intricate shape and they anyhow suffer from ohmic losses, which can dampen their EM response and hinder their up-scaling to higher frequencies. That being the case, all-dielectric MS are gaining ground also in the context of toroidal MS as a simpler technological solution with lower intrinsic losses thanks to the availability of numerous low-loss dielectric materials. An early proof-of-concept of a metastructure with toroidal response around 1 GHz exploited the high permittivity of distilled water.^[40] Periodic arrays of single or clusters of high-permittivity resonators of various shapes, for example, bars or disks, embedded in a low-index substrate offer a straightforward solution for the engineering of toroidal MS in the microwave spectrum.^[41,42] At sub-THz frequencies, we have recently demonstrated an all-silicon MS with a strong toroidal dipole resonance by using a single microfabrication process, consisting in the wet anisotropic etching of a high-resistivity floating zone silicon wafer.^[43] At infrared and optical frequencies, toroidal MS can be fabricated by lithographic definition of high-index materials, such as silicon or titanium dioxide.^[35,36]

In this work, we theoretically and experimentally demonstrate a not yet explored functionality of toroidal MS, namely, angular-dependent resonant polarization beam splitting (PBS) in the microwave K-band. The metasurface is composed of a square periodic array of high-permittivity, low-loss ceramic resonators, embedded in a 3D-printed polylactic acid (PLA) substrate. We have opted for this substrate in order to demonstrate the capability of rapid prototyping and large-scale

fabrication of the investigated PBS-MS, since PLA is one of the most common 3D-printing polymers. By proper selection of the resonator geometry, the MS exhibits a toroidal dipole resonance with a highly asymmetric Fano spectral profile in the vicinity of 20 GHz. In addition, thanks to the particular resonant electric field distribution, the MS shows very low (high) dispersion of the p-(s)-polarized mode, as demonstrated by both full-wave and band structure simulations. This property allows for the tunable relative shift of the transmittance profile for the two polarizations of the impinging plane wave by adjusting its angle of incidence through mechanical rotation of the MS. Extensive functionalities are demonstrated, such as tunable switching between PBS and bandstop or bandpass operation. The theoretical results are corroborated by microwave measurements in an anechoic chamber of two fabricated MS prototypes. The key PBS performance metrics (insertion losses, extinction ratio, and bandwidth) are evaluated and guidelines are discussed in order to further suppress insertion losses and adjust on demand the working bandwidth. Apart from providing further physical insight on the properties of toroidal dipole resonances, such MS can be deployed as polarization-control components in wireless communication systems, for example, for 5G or satcom.

2. Metasurface Layout and Operation Principle

The layout of the investigated all-dielectric metasurfaces is schematically depicted in **Figure 1a**. The metasurface is composed of a square periodic array of high-permittivity, low-loss ceramic resonators (E7324 by Exxelia),^[44] which are embedded in a PLA substrate that provides mechanical support. The pitch of the periodic lattice is p and the resonator dimensions are a (width), b (length), and h (thickness). The substrate thickness t is larger than h so as to accommodate the resonators. The PLA substrate is fabricated by a 3D-printing process, as shown in **Figure 1d**, whose details are provided in Section S1, Supporting Information. The metasurface is assembled by pressing the cuboid resonators into the equivalent cases of the PLA substrate. The target working frequency of the metasurfaces is in the microwave K-band (18–27 GHz).

In what follows, the values of the following set of parameters are selected as: $a = 4.6$ mm, $h = 1$ mm, $t = 2$ mm, and $p = 7.7$ mm. The analysis focuses on two metasurface designs that employ resonators with square ($a = b = 4.6$ mm) and rectangular ($a = 4.6$ mm, $b = 5$ mm) cross-sections, hereinafter referred to as symmetric metasurface (SMS) and asymmetric metasurface (AMS), respectively. These parameter values have been selected such that the target functionality, namely, angular-dependent PBS, is achieved, as it will be demonstrated. The relative complex permittivity of the ceramic resonators^[44] is $\epsilon_c = 24.4(1 - j4.35 \times 10^{-5})$ whereas that of the PLA substrate equals $\epsilon_s = 2.685(1 - j0.01)$. This value was retrieved by characterizing a solid plate of the used 3D-printed material through X-band waveguide measurements (details in Section S2, Supporting Information), and it is aligned with other reported measurements of PLA permittivity.^[45,46] The measured loss tangent of 0.01 is in the order of standard microwave substrates, such as FR4. A detailed analysis on the effect of the substrate

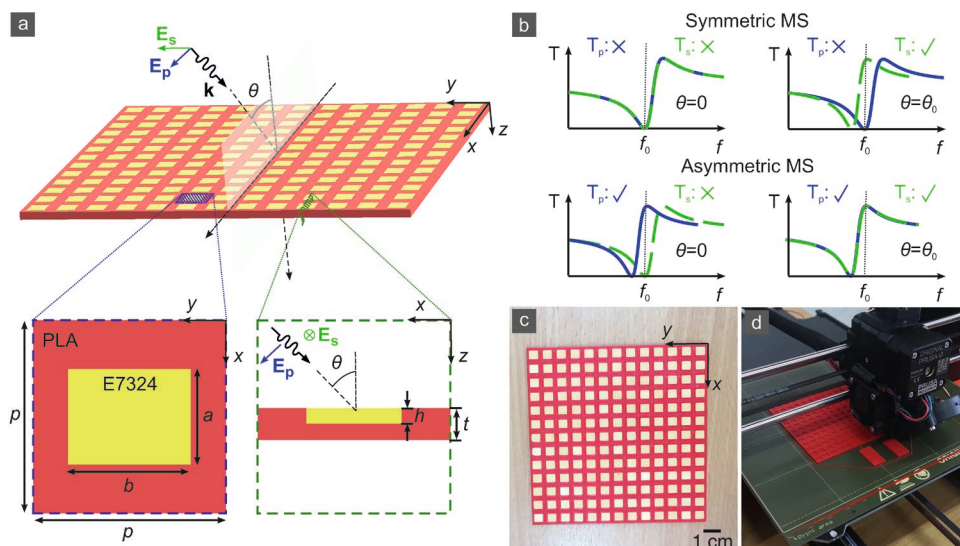


Figure 1. a) Schematic layout of the all-dielectric metasurface and definition of the coordinate axes, the plane of incidence (xz -plane), and the polarization of the impinging plane wave. The metasurface is a square periodic array (the pitch equals p) of ceramic resonators (E7324) with dimensions $a \times b \times h$ embedded in a PLA substrate of thickness t , as shown in the zoomed insets. b) Principle of the polarization beam-splitting operation of the investigated symmetric and asymmetric metasurfaces. c) Photograph of the fabricated asymmetric metasurface ($a = 4.6$ mm, $b = 5$ mm, $h = 1$ mm, $t = 2$ mm, $p = 7.7$ mm) composed of 13×13 unit cells. d) Snapshot taken during the 3D-printing process of the PLA substrate.

dielectric losses will be provided in Section 5. Figure 1c shows a photograph of the fabricated AMS, composed of an array of 13×13 unit cells.

The MS is illuminated by a plane wave impinging at an angle of incidence θ in the xz -plane, according to the definition of the reference frame in Figure 1a. Hence, the wavevector equals $\mathbf{k} = k_0(\cos\theta\mathbf{z}_0 - \sin\theta\mathbf{x}_0)$, where $k_0 = 2\pi/\lambda$ is the free-space wavenumber at the wavelength λ . Both polarizations of the electric field are investigated, namely, p- [$\mathbf{E}_p = E_0(\cos\theta\mathbf{x}_0 + \sin\theta\mathbf{z}_0)$] and s-polarization ($\mathbf{E}_s = E_0\mathbf{y}_0$).

The operation principle of the PBS-MS is illustrated in Figure 1b. In the case of the SMS, the transmittance spectra for both polarizations of a normally impinging plane wave are identical due to symmetry. It has been previously shown that when the aspect ratio (a/h) of the high-permittivity resonators is in the range here investigated, the transmittance spectrum of the resulting metasurface exhibits a strongly asymmetric Fano profile around the toroidal dipole resonant frequency.^[43,47] The transmittance minimum, common for both polarizations, dictates the working frequency. In the case of oblique incidence, the transmittance spectrum for a p-polarized wave does not undergo significant variations, thanks to the very low angular dispersion of the associated mode of the structure, as it will be demonstrated in Sections 4 and 5. On the contrary, the spectrum for an s-polarized wave shifts progressively to lower frequencies as the angle of incidence increases. At a particular angle θ_0 the transmittance extinction ratio between the two polarizations is maximized at the working frequency. Therefore, the SMS switches between operation as a band-stop filter and a polarization beam splitter at $\theta = 0$ and $\theta = \theta_0$, respectively.

In the case of the AMS, the response for normal incidence is polarization dependent. By exploiting the close spectral proximity of the transmittance minimum and maximum in the

Fano spectrum, the resonator cross-section is adjusted so as to induce a relative spectral shift of the two polarization-dependent spectra at normal incidence. This is easily achieved thanks to the asymmetric Fano profile and it is a feature exploited in other contexts as well, for instance in the design of nonlinear isolators.^[48] For a certain ratio of a/b , the transmittance minimum frequency for s-polarized matches the maximum for p-polarized wave, enabling PBS operation. Consequently, by raising the angle of incidence the transmittance spectrum of the s-polarized wave approaches that of the p-polarization until the transmittance is maximized for both polarizations at the working frequency. Hence, the AMS switches its operation from PBS at $\theta = 0$ to a bandpass filter at $\theta = \theta_0$. The details of the angular-dependent PBS spectral response of the investigated MS are elaborated in the next sections.

3. All-Dielectric Metasurfaces with Polarization-Dependent Toroidal Dipole Resonances

3.1. Scattering and Anapole States in Isolated Ceramic Resonators

Before proceeding to the analysis of the investigated MS, it is insightful to study the scattering properties of their constituent elements, namely the high-permittivity ceramic resonators. For this purpose, we employ the finite-element method (FEM) in the scattered-field formulation (COMSOL Multiphysics) in order to calculate the electric field and the polarization current in the resonator volume when it is illuminated with a normally impinging plane wave as shown in Figure 2a. Then, the multipole decomposition method in Cartesian coordinates is evoked with the aim to calculate the scattering cross-sections (SCS) of the dominant electric, magnetic, and

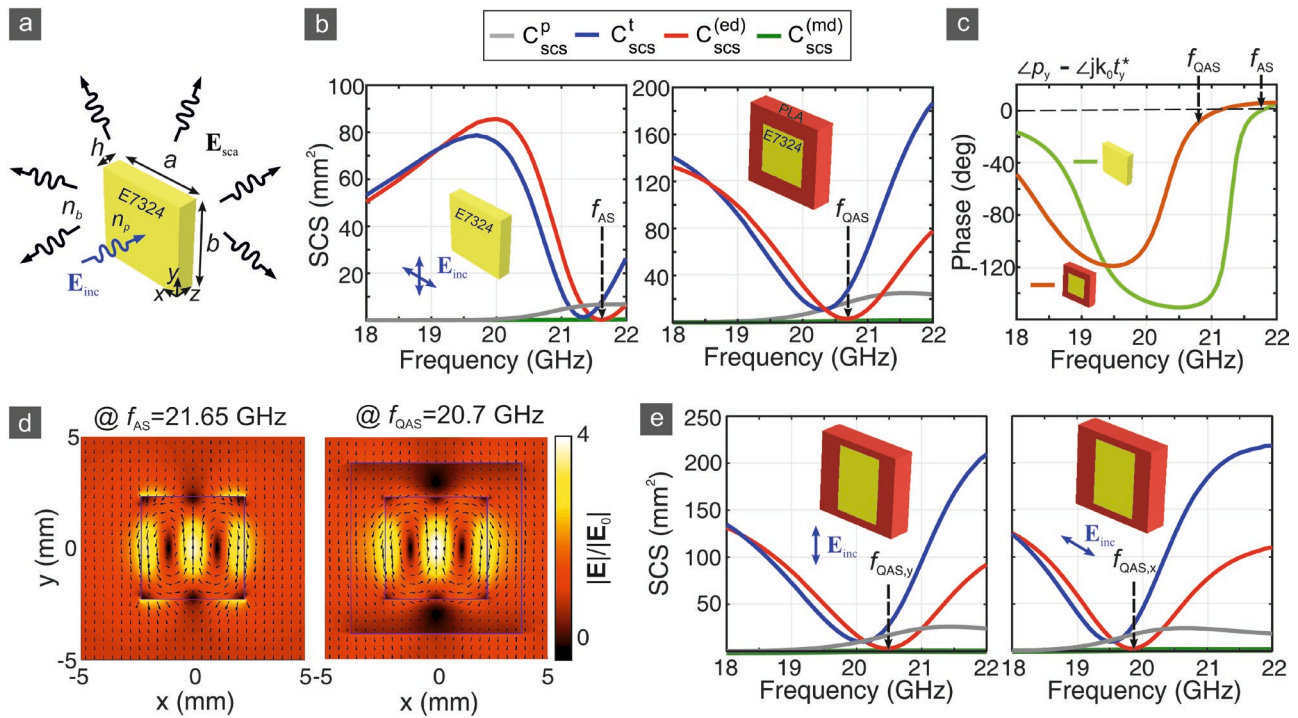


Figure 2. a) Scattering problem of an isolated ceramic resonator for a normally impinging plane wave. b) Scattering cross-sections for the Cartesian electric (p), toroidal (t), total electric (ed), and magnetic (md) dipoles of a ceramic resonator with $a = b = 4.6$ mm and $h = 1$ mm with and without the PLA frame. The anapole (quasi-anapole) state manifests at $f_{AS} = 21.65$ GHz ($f_{QAS} = 20.7$ GHz) for the case without (with) the PLA frame. c) Phase difference between the Cartesian electric dipole moment and the toroidal dipole moment for both cases. d) Spatial profile of the electric field enhancement at the anapole and quasi anapole state frequencies calculated at the mid-plane section of the ceramic resonator. e) Scattering cross-sections for the dipole moments of a ceramic resonator with $a = 4.6$ mm, $b = 5$ mm, and $h = 1$, for the two polarizations of a normally impinging plane wave. In all cases including the PLA frame, its dimensions are 7.7 mm \times 7.7 mm \times 2 mm, corresponding to the unit cell layout of Figure 1a.

toroidal multipoles (details provided in Section S3, Supporting Information).

The first investigated case deals with the scattering from a square cross-section ceramic resonator ($a = b = 4.6$ mm, $h = 1$ mm) and the corresponding results are presented in Figure 2b. The multipoles with non-negligible contribution are the electric, toroidal, and magnetic dipole. Thanks to the employed decomposition method, the separate contributions of the Cartesian electric dipole (p) and toroidal dipole (t) moments are calculated. The crossing point of their SCS spectra C_{sca}^p and C_{sca}^t , in addition to the associated cancellation of the total electric dipole SCS (C_{sca}^{ed}), marks the frequency of the so-called anapole state,^[49] which is observed at $f_{AS} = 21.65$ GHz. In particular, the total electric dipole SCS is given by (see Section S3, Supporting Information)

$$C_{sca}^{(ed)} = \frac{k_0^4}{6\pi\epsilon_0^2} |\mathbf{p} - jk_0 \mathbf{t}^*|^2 \quad (1)$$

where \mathbf{p} and \mathbf{t}^* are the Cartesian electric and corrected toroidal dipole moments, respectively, and their individual SCS are calculated as

$$C_{sca}^p = \frac{k_0^4}{6\pi\epsilon_0^2} |\mathbf{p}|^2, \quad C_{sca}^t = \frac{k_0^6}{6\pi\epsilon_0^2} |\mathbf{t}^*|^2 \quad (2)$$

The condition for the anapole state to manifest is that the Cartesian electric and toroidal dipole moments are out of phase

$\mathbf{p} = jk_0 \mathbf{t}^*$ and hence interfere destructively,^[50] or equivalently $C_{sca}^p = C_{sca}^t$ and $\angle p_y = \angle jk_0 t_y^*$, assuming without loss of generality a y -polarized impinging plane wave. It is remarked that here by “anapole” we refer to the nontrivial electric dipole anapole state. Anapole states can also manifest through the interference of other multipole moments.^[51] The anapole phase-matching condition for the investigated ceramic resonator is examined in Figure 2c.

In order to investigate the effect of the PLA substrate, the second example concerns the same resonator embedded in a PLA block with total dimensions $p \times p \times t$, which corresponds to an isolated unit cell of the investigated metasurfaces, shown in the inset of the right panel of Figure 2b. In this case, the anapole condition is not fulfilled, yet a quasi-anapole frequency can be defined at the frequency $f_{QAS} = 20.7$ GHz where C_{sca}^{ed} is minimized. This is attributed to the presence of the PLA block, which reduces the permittivity contrast between the ceramic resonator and its surrounding medium. Nevertheless, when dielectric particles with such non-pure anapole states are placed in a periodic MS configuration strong dipole resonances can still be excited thanks to collective oscillations from the coupling among adjacent particles.^[34]

Further evidence on the presence of the anapole state is provided in Figure 2d, where the electric field profile at the mid-plane of the resonator along the z -axis is depicted. The observed opposing loops of electric field lines/displacement current are a distinctive feature of the dipole anapole state. It

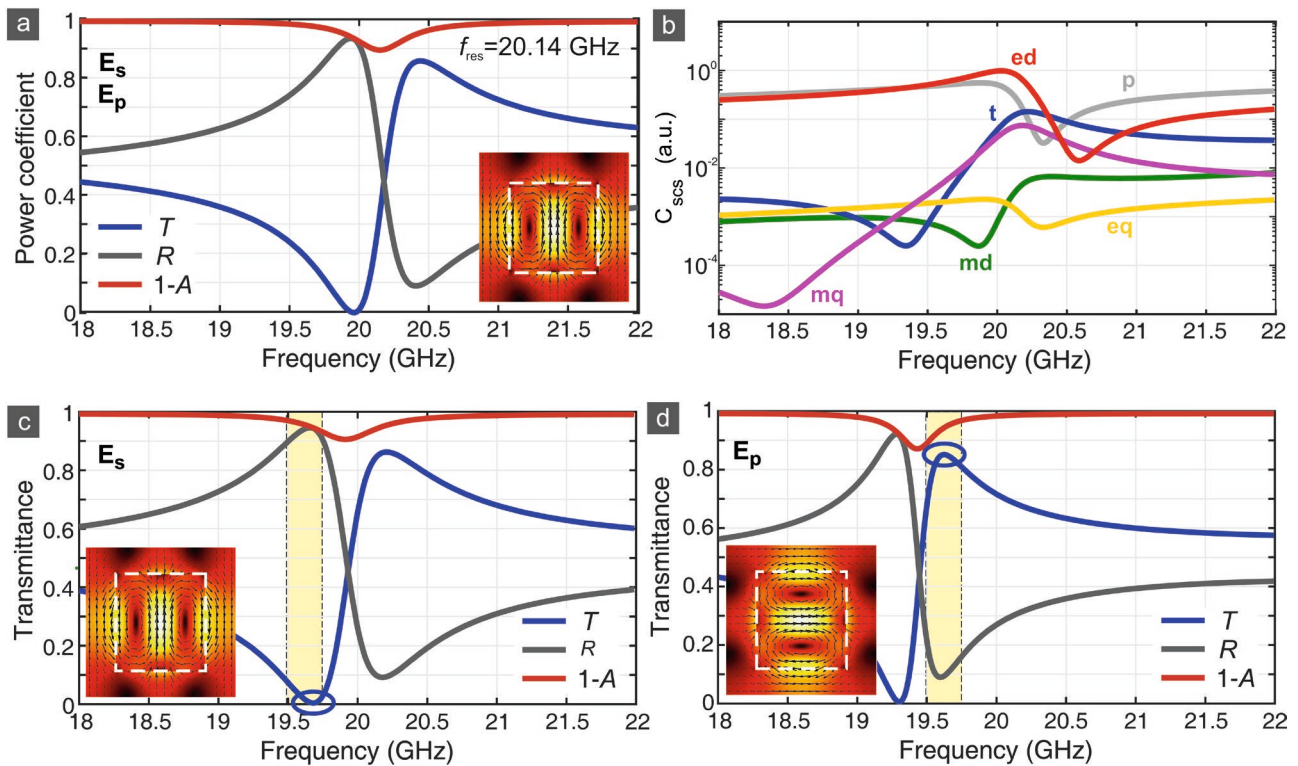


Figure 3. a) Transmittance (T), reflectance (R), and absorptance ($A = 1 - R - T$) spectra for the investigated symmetric metasurface for a normally incident plane wave. The inset shows the spatial profile of the electric field at the resonant frequency $f_{\text{res}} = 20.14$ GHz. b) Relative scattering power of the Cartesian electric (p), toroidal (t), total electric (ed), magnetic (md) dipoles, and the electric (eq) and magnetic (mq) quadrupoles. Transmittance, reflectance, and absorptance spectra for the investigated asymmetric metasurface at normal incidence for a c) s-polarized and d) p-polarized normally incident plane wave. The transmittance minimum for the case of s-polarized wave is observed at the same frequency as the transmittance maximum for the case of p-polarized wave. The insets show the electric field profiles at the corresponding resonant frequencies $f_{\text{res}}^s = 19.91$ and $f_{\text{res}}^p = 19.42$ GHz.

is interesting to remark that the electric field is mainly concentrated in three regions along the x -axis, that is, perpendicular to the polarization axis of the y -polarized impinging plane wave. This characteristic is key to understanding the scattering behaviour from the rectangular cross-section resonator ($a = 4.6$ mm, $b = 5$ mm, $h = 1$ mm) embedded in the same PLA block, which is studied in Figure 2e. The SCS spectra for the dipole moments show similar trends, apart from an overall spectral shift for the case of x -polarized electric field. Such red-shifting, that is, toward lower frequencies, is expected when the electric field probes a larger portion of the high-permittivity material. Although the long axis of the resonator is parallel to the y -axis, the spectra are red-shifted for the plane wave of perpendicular polarization. This is explained by observing the high-field concentration regions of the profiles in Figure 2d.

3.2. Asymmetric Fano Toroidal Resonances in All-Dielectric Metasurfaces

The investigated metasurfaces are composed of a periodic array of the ceramic resonator/PLA substrate unit cells studied in Figure 2. The analysis focuses on two particular designs of SMS and AMS, whose geometrical parameters were described in Section 2. The case of a normally incident plane wave is first

investigated. **Figure 3a** shows the SMS transmittance, reflectance, and absorptance spectra, which do not depend on the polarization of the incident wave due to fourfold symmetry of the MS unit cell's cross-section. The spectra exhibit a characteristic asymmetric Fano profile, with a resonant frequency of $f_{\text{res}} = 20.14$ GHz and a quality factor $Q = 44$, as calculated by fitting the simulated spectra to a generic Fano function found to accurately reproduce the results (details in Section S4, Supporting Information). The Fano resonant frequency coincides with the frequency where absorptance is maximized ($A_{\text{max}} = 10.8\%$), stemming almost exclusively from absorption losses in the PLA substrate. The maximum absorptance in the ceramic resonators is 0.2%, thanks to the very low losses of the ceramic material.

The inset of Figure 3a shows the electric field profile at the resonant frequency for an s-polarized incident wave. The field distribution is similar to the profiles of the isolated unit cell at the anapole frequency, as in Figure 2d, which is an indication of the toroidal dipole nature of the resonance. Again, it is important to notice that the electric field lobes are aligned along the axis perpendicular to the impinging polarization. In addition, higher field localization in the PLA volume among the resonators, which hints for the potential of intense coupling, is also observed along the x -axis. The strong toroidal contribution is further corroborated by the results of Figure 3b, where the relative scattering power of the various multipole moments

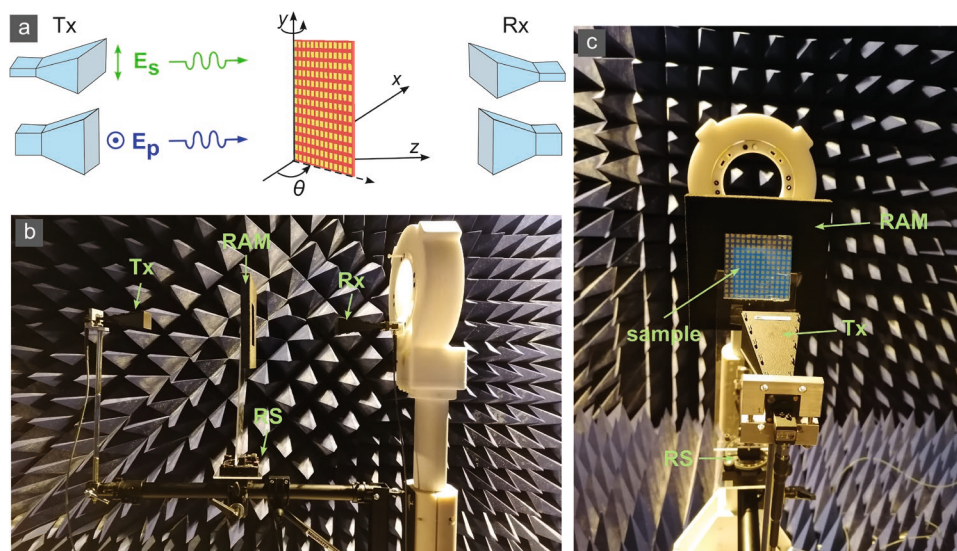


Figure 4. a) Schematic layout of the experimental setup for the characterization of the metasurfaces in the K-band. The angle of incidence is adjusted by mounting the sample on a rotation stage (RS). The polarization of the incident wave is selected by rotating by 90° the Rx and Tx horn antennas. This configuration is equivalent to the layout presented in Figure 1a. The y-axis is aligned with the length b of the resonators. b) Photograph of the experimental setup, showing the entire link including the transmit (Tx) and receive (Rx) horn antennas, the sample placeholder, that is, a slab made of radar absorbing material (RAM) with a square opening and the RS. The complete experimental setup is accommodated within an anechoic chamber. c) Photograph taken from the perspective of the Tx antenna, showing the sample mounted in the RAM placeholder.

is calculated. Apart from the dominant electric and toroidal dipoles, the quadrupole magnetic moment also has a non-negligible contribution. It is noted that these results are produced by decomposing the fields in a single unit cell of the MS, which are computed by full-wave simulations with the application of the necessary periodic boundary conditions.^[52,53]

The response of the AMS and the electric field profiles on resonance are investigated in Figure 3c,d for an s- and p-polarized normally impinging plane wave. The corresponding Fano resonant frequencies are $f_{\text{res}}^s = 19.91$ GHz, $f_{\text{res}}^p = 19.42$ GHz, and $Q^s = 38.5$ and $Q^p = 62.7$. It is observed that the resonant frequency for p-polarization, namely x-polarized wave in the case studied, is lower ($f_{\text{res}}^p < f_{\text{res}}^s$). Given the similarity of the field profiles shown in Figures 3 and 2d, this behavior is attributed, as in the scattering problem from the isolated resonators, to the higher electric field concentration along the axis perpendicular to the polarization axis of the impinging plane wave. This characteristic is important for the tunable PBS operation of the AMS, as it will be clarified in Sections 4 and 5. The results of the multipole decomposition for the two polarization cases of the AMS show similar behavior to Figure 3b, and they are reported for completeness in Section S3, Supporting Information.

As evidenced from the transmittance spectra in Figure 3c,d, the AMS operates in PBS mode for normal incidence. The resonator length/width ratio (b/a) is selected such that the minimum transmittance frequency for s-polarization matches that of maximum transmittance for p-polarization. In the case of the AMS, this occurs at the working frequency of $f_{\text{op}} = 19.65$ GHz. It is convenient to quantify a metric with respect to the operation bandwidth of the PBS-AMS, here defined as the spectral window where an extinction ratio (ER) above 10 dB is achieved between the two polarization, namely f : $\text{ER} \equiv \log_{10}[T_p(f)/T_s(f)] > 10$ dB.

The bandwidth of the AMS is 300 MHz and it extends from 19.48 to 19.78 GHz, marked as the yellow shaded region in Figure 3c,d.

The experimental evaluation of the two fabricated MS was conducted in an anechoic chamber, using a pair of standard gain 20 dBi, K-band (17.6–26.7 GHz) horn antennas (FLANN Microwave 20240) and a Vector Network Analyzer (Anritsu 37397D). The layout of the antenna measurements and two actual views of the employed measurement setup are shown in Figure 4. The sample is mounted on a lightweight plastic frame, which is subsequently attached to a square opening, cut on a slab made of radar absorbing material (RAM), in order to eliminate spurious diffraction effects. The plastic frame is mounted on a rotation stage (RS), which controls the angle of incidence of the impinging plane wave. In addition, the polarization of the incident wave is controlled by rotating the pair of transmit (Tx) and receive (Rx) antennas by 90° , as schematically shown in Figure 4a. This configuration allows for the full characterization of the investigated MS. In order to record the sample transmittance spectra, each measurement corresponding to different polarization and/or angle of incidence is referenced to the signal measured in the absence of the sample, namely with the placeholder and RAM frame mounted as shown in Figure 4b. A view taken from the perspective of the Rx antenna is shown in Figure 4c. The sample corresponds to the SMS and it was printed in blue PLA that comes from the same manufacturer as the red one seen in Figure 1; both share identical electrical properties (the color serves only purposes of visual differentiation). The slight discoloration seen in the substrate material surrounding the left two columns and upper three rows of resonators is due to the light illumination (a light spot is mounted on the anechoic chamber ceiling corner) that is shaded by the RAM slab edges.

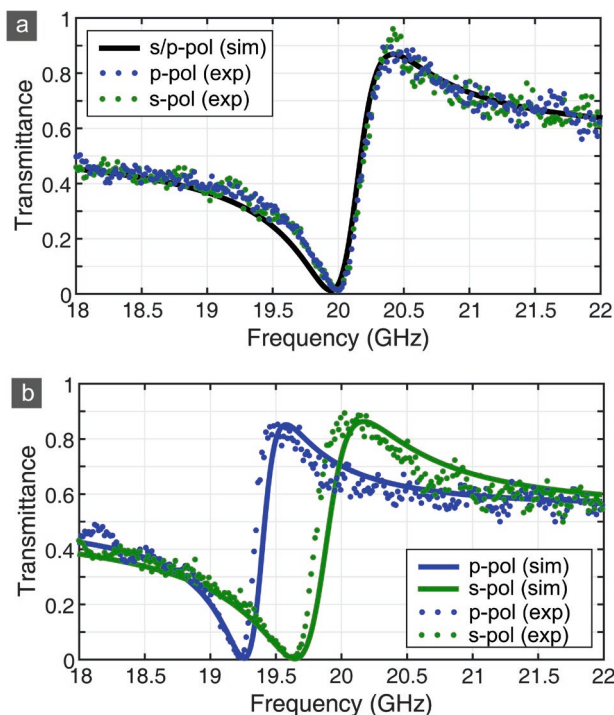


Figure 5. Theoretically calculated and experimentally measured transmittance spectra for both polarizations of a normally incident wave for the a) symmetric and b) asymmetric metasurface.

Figure 5 shows a direct comparison between the theoretically simulated and the experimentally measured transmittance spectra of the two MS. Excellent agreement is observed in terms of both the resonant frequencies and the asymmetric shape of the Fano linewidth. The PBS properties of the AMS are demonstrated with a measured extinction ratio of 22 dB at the working frequency. In addition, the theoretically expected polarization-independent electromagnetic response of the SMS is also experimentally corroborated.

4. Angular-Dependent Polarization Beam Splitting and Filtering

Next, we investigate the angular-dependent PBS performance of the two designed MS. The transmittance spectra for both MS are first theoretically simulated for an angle of incidence θ varying from 0 to 45°. The results are concisely presented in the transmittance maps of Figure 6a. The white dashed lines mark the Fano resonant frequencies and they outline their dependence on the angle θ . It is interesting to remark that the resonant frequency for the p-polarization in the case of both MS shows negligible dependence on θ , that is, negligible spatial dispersion. On the contrary, the resonance for s-polarized waves exhibits a progressive shift toward lower frequencies for increasing θ , demonstrating the behavior of a spatial frequency filter.^[54]

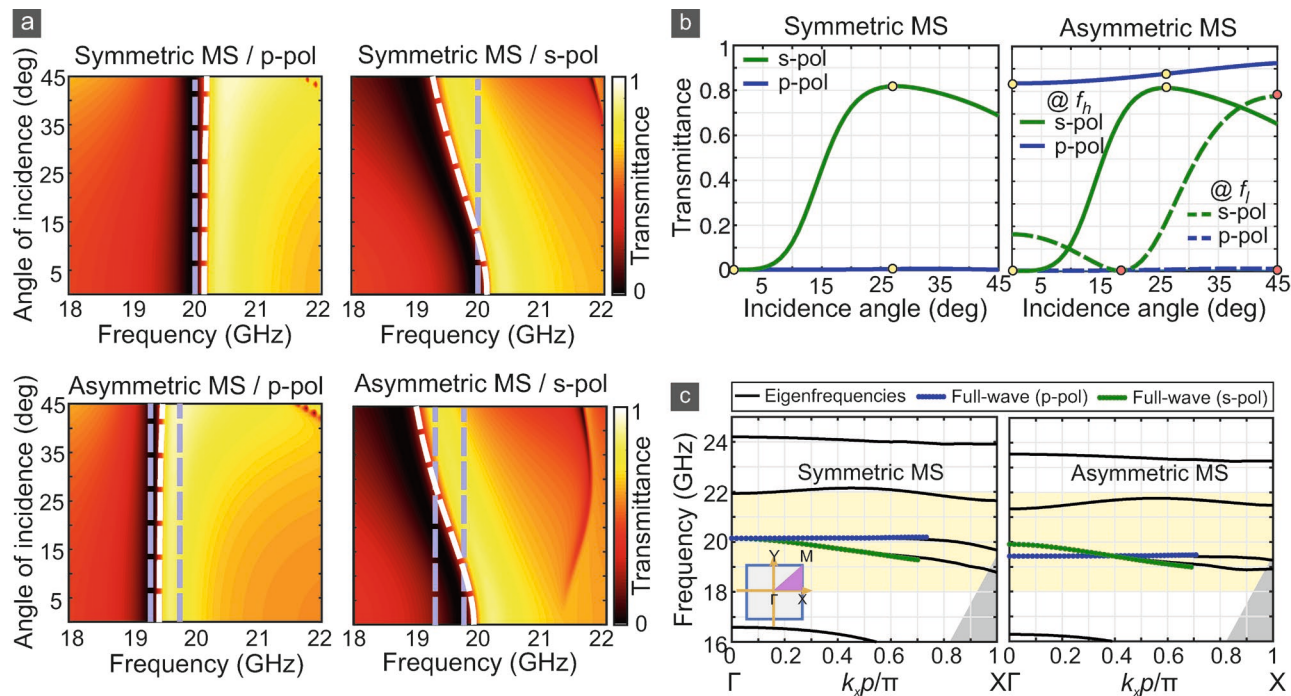


Figure 6. a) Maps of the transmittance spectra for the symmetric and asymmetric metasurfaces for an angle of incidence varying from 0 to 45° for the s- and p-polarizations of the impinging plane wave. The white dashed lines mark the resonant frequencies resulting from the Fano fitting of the spectra and the grey dashed lines the working frequencies [$f_{op} = 19.93$ GHz (SMS), $f_p = 19.65$ GHz and $f_s = 19.29$ GHz (AMS)]. b) Transmittance for both metasurfaces and wave polarizations at the working frequencies as a function of the angle of incidence. c) Band diagrams for both metasurfaces in the investigated spectral window along the $\Gamma \rightarrow X$ direction of the irreducible Brillouin zone of the square periodic arrays. The dots are the equivalent points calculated from the resonant frequencies of (a).

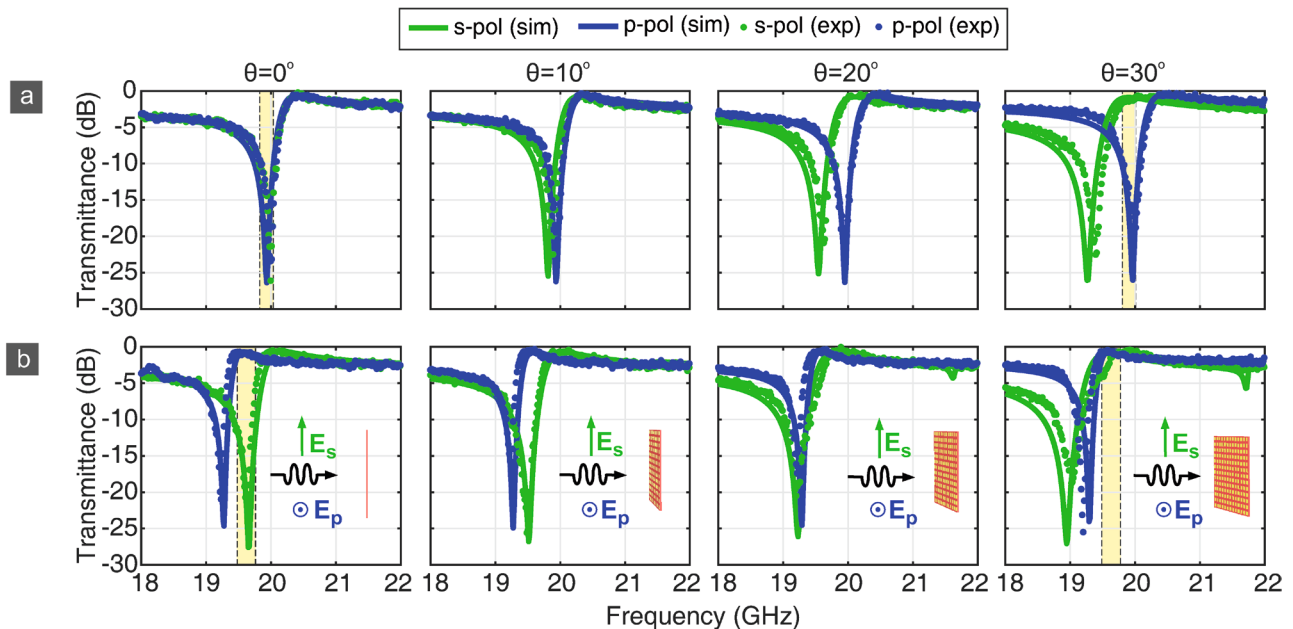


Figure 7. Theoretically calculated and experimentally measured transmittance spectra for both polarizations of the incident wave for the a) SMS and b) AMS for an angle of incidence from 0 to 30° in steps of 10°. The yellow shading marks the operation bandwidth for the two cases.

This behavior is key to achieving the target PBS angular-dependent performance, which provides tunable operation by mechanical rotation. In the case of the SMS, the transmittance $T_p(f_{op})$ stays very low in the entire range of values for θ . The working frequency ($f_{op} = 19.93$ GHz) corresponds to minimum transmittance at $\theta = 0^\circ$ (equal for both polarizations) and it is marked with a gray dashed line in Figure 6a. Due to the progressive shift of the spectra T_s , the transmittance for s-polarized wave increases at the working frequency, until it reaches a maximum value at $\theta = \theta_0$. The angle- and polarization-dependent transmittance at f_{op} is evaluated in Figure 6b. The PBS angle is equal to $\theta_0 = 27^\circ$, at which the transmittance for the two polarizations is $T_s(f_{op}, \theta_0) = 81\%$ and $T_p(f_{op}, \theta_0) = 0.5\%$. The PBS bandwidth is calculated at θ_0 and it is found equal to 220 MHz, extending from 19.83 to 20.05 GHz. Therefore, the SMS switches between a bandstop ($\theta = 0$) and a PBS state ($\theta = 27^\circ$) by simple mechanical in-plane rotation. The transmittance values T_p and T_s at both states are marked as yellow spots in Figure 6b for clarity. Nevertheless, the transition is continuous, therefore the transmittance of the s-polarized wave can be modulated between its minimum and maximum value by adjusting the angle θ .

In the case of the AMS, it has been demonstrated in Section 3.2 that PBS is achieved for normal incidence at the working frequency $f_h = 19.65$ GHz. For an increasing angle of incidence, the transmittance $T_p(f_h, \theta)$ is slowly enhanced, from approximately 80% at $\theta = 0$ to 90% at $\theta = 45^\circ$, as shown in Figure 6b. As far as the s-polarized wave is concerned, its resonant frequency red-shifts, crosses the working frequency f_h at approximately $\theta = 15^\circ$ and further diverges for increasing θ . This spectral shift leads to a modulation of the s-wave transmittance from $T_s(f_h) = 0$ to 82% for θ varying from 0° to 27° . Thus, the AMS switches between PBS ($\theta = 0^\circ$) and bandpass operation ($\theta = 27^\circ$).

It is interesting to observe that the AMS provides also for a second possibility of mechanically tunable PBS. Apart from the working frequency f_h as defined in Section 3.2, tunable PBS is also achieved at a second, lower, working frequency $f_i = 19.29$ GHz, which coincides with the transmittance minimum of p-polarized wave at normal incidence. At that frequency, $T_p(f_i, \theta)$ remains very low, while $T_s(f_i, \theta)$ starts at a value of 16% for normal incidence, drops to a zero minimum at $\theta_1 = 18^\circ$, and then increases monotonically to the value of 80% at $\theta_2 = 45^\circ$. Hence, the AMS switches its operation at f_i from bandstop ($\theta = \theta_1$) to PBS ($\theta = \theta_2$), and therefore it provides the same functionality of the SMS, albeit at different PBS angles and with a lower bandwidth of 140 MHz (additional information in Section S5, Supporting Information).

The angular-dependent PBS properties of the MS were experimentally tested for an indicative set of values for the angle of incidence, from $\theta = 0^\circ$ to 30° with an increment of 10° . The measurement results presented in Figure 7 confirm all the trends of the MS: the angle-insensitivity for p-polarization, the gradual red-shift for the s-polarization for increasing θ and the bandstop, bandpass and PBS operation at the corresponding working frequencies of the two MS. Some discrepancy between measurements and experimental results at higher angles is attributed to the finite size of the MS and the reduction at oblique incidence of the effective surface that interacts with the incident plane wave, as well as the tolerance in the dimensions of the fabricated resonators, declared at 50 μm by the manufacturer.

5. Discussion and Conclusions

As explained in the previous sections, the PBS performance of the investigated metasurfaces relies on a series of features: a) the MS assembling from high-permittivity, low-loss ceramic

resonators that provide rich opportunities to harvest Mie multipole resonances; b) the design of the MS dimensions such that a toroidal dipole resonance is induced close to the anapole state frequency of the individual resonators; c) the strongly asymmetric Fano profile of the resulting toroidal resonance, which makes straightforward the design of rectangular cross-section resonators for PBS at normal incidence; d) the very low (high) sensitivity of the MS response on the angle of incidence for p-(s)-polarized wave.

With the aim to further elucidate on the observed differences in the polarization-dependent angular dispersion, we have calculated the band structure of the periodic MS array using the FEM method by using appropriate Floquet boundary conditions and calculating the eigenfrequencies of the periodic unit cell for both SMS and AMS. The band structure is calculated for $k_y = 0$ and k_x ranging from 0 to π/p , which corresponds to the Γ to X contour path of the irreducible Brillouin zone of the square MS lattice. The results for the two MS are presented in Figure 6c, where the spectral window under investigation is marked in yellow shading. The gray region corresponds to the part below the light line, which contains guided modes of the structure. Modes above the light line can be externally excited, for instance, by an incident plane wave.

This is the case of the pair of modes of interest around 20 GHz, whose band diagram is reconstructed by calculating the in-plane wavevector $k_x = k_0 \sin \theta$ component and the corresponding Fano resonant frequencies for each of the spectra calculated in Figure 6a. The results are superimposed as blue and green dots on the band diagram, showing excellent agreement with the calculated eigenfrequencies of the MS. It is further demonstrated that the modes excited by p-polarized wave show very low dispersion up to a value of $k_x = 0.8\pi/p$, which covers the entire parameter space under investigation in the context of the tunable PBS-MS. Such angle-insensitive behavior has been recently observed in other types of microwave toroidal metasurfaces as well.^[55] On the contrary, the s-polarized mode shows significant dispersion, since the associated resonant electric field profile (inset of Figure 3a) leads to coupling between adjacent resonators along the perpendicular axis, which is enhanced for increasing k_x . It is remarked that the demonstrated MS spatially dispersive behavior stems from the properties of the individual scatterers at a fundamental level. Hence, it is not some collective effect resulting from the MS periodicity, which can be explained by analytical models such as, for instance, in the case of metallic frequency selective-surfaces.^[56,57]

The two modes are degenerate, as expected, due to symmetry at the Γ point of the SMS and their bands progressively diverge as k_x obtains higher values. On the contrary, the s-polarized mode has a higher frequency at the Γ point of the AMS with respect to the p-polarized mode. The bands of the two modes cross at approximately $k_x = 0.4\pi/p$ and then diverge. It is here remarked that in order for the AMS to exhibit PBS properties, it is essential that the plane of incidence, here the xz -plane, is perpendicular to the long axis of the ceramic resonators, namely, the y -axis. In case the plane of incidence were the yz -plane, or equivalently if $a \leftrightarrow b$, according to Figure 1a, the two modes would flip positions at the Γ point and the s-polarized mode would simply further diverge for increasing θ . Overall,

the dispersive behavior of the two modes, as revealed in the band diagram, explains from a different perspective the tunable PBS properties of the two MS studied in Section 4.

Last, the band diagram for the AMS shows a third mode within the frequency range under investigation. This mode corresponds to the resonance between 21 and 22 GHz observed in the right panel of Figure 6c. It is interesting to note that the mode is not excited at normal incidence. In fact, the mode is a bound state in the continuum (BIC),^[58,59] which is symmetry-protected at normal incidence, but becomes quasi-BIC with a finite lifetime and hence excited by obliquely incident plane waves.^[60,61] A brief analysis of its properties is provided in Section S6, Supporting Information.

Next, we discuss the key operation parameters of the investigated PBS-MS, namely: a) working frequency, b) insertion losses, and c) extinction ratio/bandwidth. The working frequency clearly depends on the geometrical parameters; however, once a working design is defined, it can be scaled for operation at a different frequency in a straightforward manner. The employed ceramic resonators feature an operation range from 7 to 40 GHz with minimal material dispersion,^[44] which covers radar, satcom, and, importantly, a large part of the 5G Frequency Range 2 (FR2) spectrum (24.25–52.6 GHz). The material dispersion of the substrate can also be very low, as here demonstrated for the case of the 3D-printed PLA material, which showed minimal dispersion in the X-band measurements, yielding a permittivity value that reproduced excellently the MS resonant frequencies around 20 GHz. In any case, given the availability of high-permittivity resonators,^[62] a fine tuning of the geometry can restore the MS-PBS performance in the case of slightly different permittivity values of the constituent materials.

As far as insertion losses (IL) are concerned, in all cases here investigated, the maximum transmittance for the pass-polarization is above 80%, namely the IL are lower than 1 dB. In Section 3.2, it has been demonstrated that the low-loss resonators marginally affect the absorption losses of the MS. Thus, a way to directly decrease the IL is to use a substrate with a lower loss tangent. In order to isolate the effect of the losses, we evaluate the PBS performance of the AMS in Figure 8a, by artificially varying the PLA loss tangent, spanning a range compatible with microwave substrates, either 3D-printable (e.g., acrylonitrile butadiene styrene and high-impact polystyrene) or standard (such as polytetrafluoroethylene at the low-loss edge).^[45,46] A loss tangent of 0.001 increases the transmittance above 90%, whereas its further reduction by one order of magnitude has negligible impact. A way to further suppress the IL is by using a low-permittivity microwave foam. Figure 8b compares the PBS performance between the fabricated AMS and an equivalent AMS with all geometric parameters equal except the resonator length, adjusted at $b = 4.8$ mm, and the substrate type, which is the Rohacell 31 microwave foam characterized by $\epsilon_r = 1.05(1 - j0.0034)$.^[63] Owing to the reduction of the substrate permittivity, the working frequency is shifted to a higher value. What is important, though, is that the maximum transmittance is above 99% considering the same ceramic resonators and a commercially available substrate. Therefore, there is ample room to reduce the IL of the investigated PBS-MS, even to a negligible level.

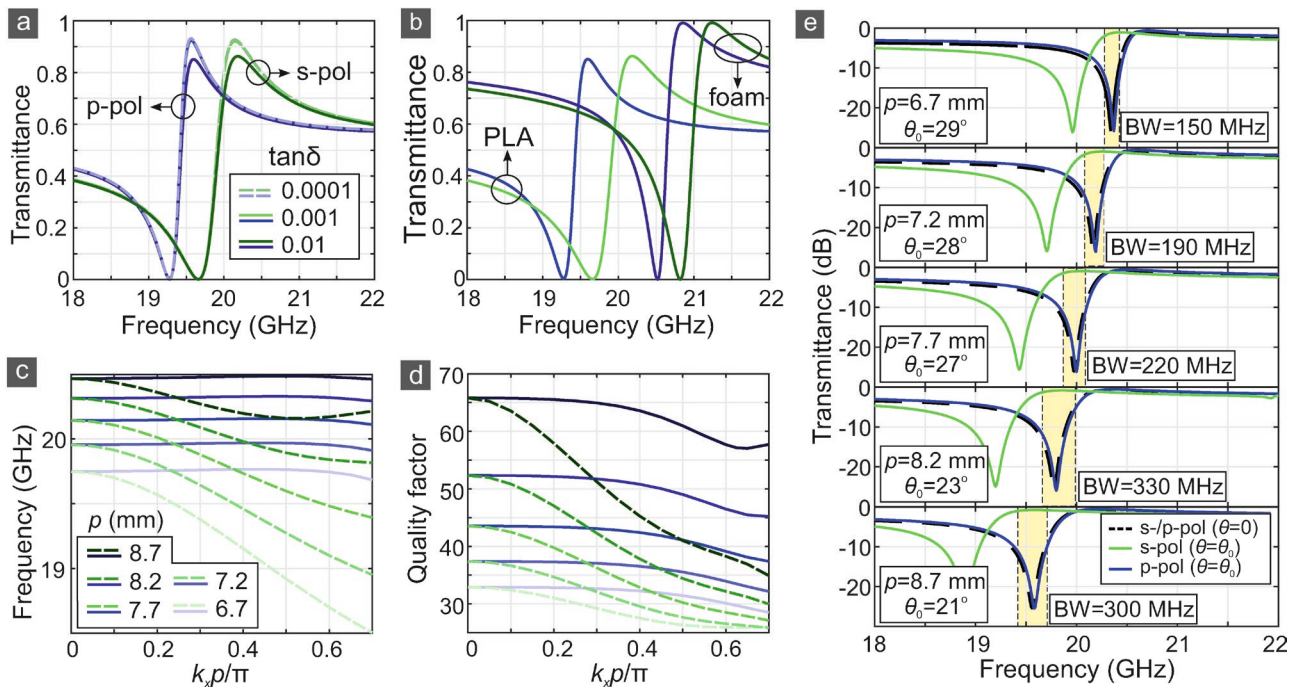


Figure 8. a) Influence of the PLA loss tangent on the PBS performance of the AMS. b) Comparison of the PBS performance of the AMS with a similar AMS employing a microwave foam substrate (Rohacell 31). c) Eigenfrequencies and d) quality factors of the pair of s-/p-polarized modes (dashed and solid lines, respectively) for a set of symmetric MS ($a = b = 4.6$ mm, $h = 1$ mm, $t = 2$ mm) with a varying pitch from 6.7 to 8.7 mm in steps of 0.5 mm. e) PBS performance of the symmetric MS as a function of the pitch.

The extinction ratio at the PBS working frequency is mainly dictated by the transmittance of the stop-polarization, which can be arbitrarily low from the theoretical point of view. However, the very high achievable ER is also experimentally demonstrated, as in Figure 7, where measured ER values higher than 25 dB are reported for the experimentally characterized finite MS.

Furthermore, the working PBS bandwidth in the cases studied is in the range of a few hundred MHz. Such values are compatible, for instance, with the maximum carrier bandwidth in the 5G-FR2 spectrum, which is set to 400 MHz.^[64] Here, we investigate a solution allowing for the adjustment of the PBS bandwidth by properly selecting the MS pitch. We consider the design of the SMS and we modify the MS pitch in the range of ± 1 mm around the value of $p = 7.7$ mm. The complex eigenfrequencies $\tilde{\omega}$ for the set of investigated s-/p-polarized modes are calculated by FEM and the modal dispersion curves and corresponding quality factors, equal to $Q = \Re\{\tilde{\omega}\} / 2\Im\{\tilde{\omega}\}$,^[65] are shown in Figures 8c and 8d, respectively. Shorter pitch values lead to higher modal frequencies, as the high-permittivity resonators occupy a higher volume fraction and higher quality factors due to stronger interaction among adjacent resonators. The very low dispersion for the p-polarized mode is verified in all examples investigated.

Instead of resorting to a full-scale investigation of each structure as a function of the angle of incidence θ , we estimate to a first approximation the PBS working θ_0 based on the results of Fig 8c,d. In order to achieve PBS at the working frequency f_{op} , namely, the minimum transmittance frequency at normal incidence, the transmittance spectrum for the s-polarization needs

to be red-shifted by a factor of 2γ , where γ is the linewidth of the Fano resonance, or, equivalently, $\Delta f^s = f_{op}(1 - 1/Q)$. Then, the working k_x point is identified in Figure 8c and the working angle of incidence is calculated as $\theta_0 = \arcsin(k_x/k_0)$, where $k_0 = 2\pi f_{op}/c_0$ and c_0 the speed of light in vacuum. This approach does not take into account the variation of the quality factor for the s-polarized mode; however, it provides satisfactory results, as shown in Figure 8e. The bandwidth can be adjusted by at least a factor of two, which demonstrates the versatility of the PBS-MS in applications requiring a precise sub-GHz working bandwidth.

Overall, the proposed PBS provides a novel solution for polarization control at microwave frequencies, including the rapidly researched millimeter-wave bands. As discussed, the IL can be minimized by using standard low-permittivity substrates. This is particularly relevant in view of applications at higher millimeter-wave frequencies, as current metasurface-based PBS, which are designed for static operation, employ metallic elements with the associated loss issues.^[66,67] The ER is very high owing to the spectral shape of the asymmetric Fano resonance and the bandwidth is compatible with envisaged applications such as 5G wireless links. The PBS is low-profile, thanks to the subwavelength MS thickness. The latter is practically defined by the ceramic resonator thickness (the dielectric substrate can be thinned down), namely 1 mm, which is $\approx \lambda/15$. Using even higher-permittivity resonators^[44] could push the MS thickness to even lower values. The MS fabrication does not involve printed-circuit board or lithographic techniques, but only a single-step mechanical assembly of the resonators in a perforated substrate, which is promising for automated and

large-scale manufacturing. Last but not least, the PBS shows tunable functionalities for polarization control through simple mechanical rotation, which is achieved at a fundamental level. As such, the PBS could be exploited in dual-polarization wireless links by splitting/combining the two linear wave components, essentially providing a free-space, tunable analog of orthomode transducers, which are broadly used, for instance, in ground or satellite links as well as in radiofrequency astronomy.^[68,69]

In conclusion, we have theoretically and experimentally investigated the polarization-dependent properties of an all-dielectric MS that exhibits a toroidal resonance with a highly asymmetric Fano profile around 20 GHz. By proper selection of the MS, geometry tunable PBS is demonstrated by controlling the angle of incidence of the impinging plane wave. Such performance is enabled by the very low (high) dispersion of the p(-s)-polarized mode, properties that are intrinsic to this type of MS. Finally, guidelines to improve or controllably adjust the key performance characteristics of the tunable PBS-MS, namely, working frequency, insertion losses, and bandwidth, are discussed. The proposed free-space components show extensive versatility for the polarization control of propagating radio signals in microwave bands for wireless communication, for example, 5G and satcom.

Supporting Information

Supporting Information is available from the Wiley Online Library or from the author.

Acknowledgements

This research was co-financed by the European Union and Greek national funds through the Operational Program Competitiveness, Entrepreneurship and Innovation, under the call RESEARCH CREATE INNOVATE (Project code: No. T1EDK-02784) and by the Comunidad de Madrid and FEDER Program (S2018/NMT-4326), the Ministerio de Economía y Competitividad of Spain (TEC2016-77242-C3-1-R and TEC2016-76021-C2-2-R), and the FEDER/Ministerio de Ciencia, Innovación y Universidades and Agencia Estatal de Investigación (RTC2017-6321-1, PID2019-107270RB-C21 and PID2019-109072RB-C31).

Conflict of Interest

The authors declare no conflict of interest.

Data Availability Statement

The data that support the findings of this study are available from the corresponding author upon reasonable request.

Keywords

all-dielectric metasurfaces, polarization beam splitting, polarization filtering, toroidal resonances, tunable microwave wireless components

Received: December 13, 2020

Revised: February 15, 2021

Published online:

- [1] H. T. Chen, A. J. Taylor, N. Yu, *Rep. Prog. Phys.* **2016**, *79*, 076401.
- [2] P. Genevet, F. Capasso, F. Aieta, M. Khorasaninejad, R. Devlin, *Optica* **2017**, *4*, 139.
- [3] F. Ding, A. Pors, S. I. Bozhevolnyi, *Rep. Progr. Phys.* **2017**, *81*, 026401.
- [4] S. M. Kamali, E. Arbabi, A. Arbabi, A. A. Faraon, *Nanophotonics* **2018**, *7*, 1041.
- [5] E. Arbabi, A. Arbabi, S. M. Kamali, Y. Horie, A. Faraon, *Optica* **2016**, *3*, 628.
- [6] R. Paniagua-Domínguez, Y. F. Yu, A. E. Miroshnichenko, L. A. Krivitsky, Y. H. Fu, V. Valuckas, L. Gonzaga, Y. T. Toh, A. Y. S. Kay, B. Luk'yanchuk, A. I. Kuznetsov, *Nat. Commun.* **2016**, *7*, 10362.
- [7] J. Algorri, B. García-Cámara, A. Cuadrado, J. M. Sánchez-Pena, R. Vergaz, *Nanomaterials* **2017**, *7*, 177.
- [8] N. M. Estakhri, V. Nader, M. W. Knight, A. Polman, A. Alù, *ACS Photonics* **2017**, *4*, 228.
- [9] J. Bohn, T. Bucher, K. E. Chong, A. Komar, D. Y. Choi, D. N. Neshev, Y. S. Kivshar, T. Pertsch, I. Staude, *Nano Lett.* **2018**, *18*, 3461.
- [10] S. Yuan, X. Qiu, C. Cui, L. Zhu, Y. Wang, Y. Li, J. Song, Q. Huang, J. Xia, *ACS Nano* **2017**, *11*, 10704.
- [11] A. Ferraro, D. C. Zografopoulos, M. A. Verschuuren, D. K. G. de Boer, F. Kong, H. P. Urbach, R. Beccherelli, R. Caputo, *ACS Appl. Mater. Interfaces* **2018**, *10*, 24750.
- [12] E. Arbabi, S. M. Kamali, A. Arbabi, A. Faraon, *ACS Photonics* **2018**, *5*, 3132.
- [13] Y. Yang, I. I. Kravchenko, D. P. Briggs, J. Valentine, *Nat. Commun.* **2014**, *5*, 5753.
- [14] S. Campione, S. Liu, L. I. Basilio, L. K. Warne, W. L. Langston, T. S. Luk, J. R. Wendt, J. L. Reno, G. A. Keeler, I. Brener, M. B. Sinclair, *ACS Photonics* **2016**, *3*, 2362.
- [15] S. Liu, M. B. Sinclair, S. Saravi, G. A. Keeler, Y. Yang, J. Reno, G. M. Peake, F. Setzpfandt, I. Staude, T. Pertsch, I. Brener, *Nano Lett.* **2016**, *16*, 5426.
- [16] P. P. Vabishchevich, S. Liu, M. B. Sinclair, G. A. Keeler, G. M. Peake, I. Brener, *ACS Photonics* **2018**, *5*, 1685.
- [17] N. Papasimakis, V. A. Fedotov, V. Savinov, T. A. Raybould, N. I. Zheludev, *Nat. Mater.* **2016**, *15*, 263.
- [18] I. B. Zel'dovich, *J. Exp. Theor. Phys.* **1957**, 1184.
- [19] W. C. Haxton, *Science* **1997**, *275*, 1753.
- [20] C. M. Ho, R. J. Scherrer, *Phys. Lett. B* **2013**, *722*, 341.
- [21] N. A. Spaldin, M. Fiebig, M. Mostovoy, *J. Phys: Condens. Matter* **2008**, *20*, 434203.
- [22] V. R. Tuz, V. V. Khardikov, Y. S. Kivshar, *ACS Photonics* **2018**, *5*, 1871.
- [23] Y. He, G. Guo, T. Feng, Y. Xu, A. E. Miroshnichenko, *Phys. Rev. B* **2018**, *98*, 161112(R).
- [24] V. R. Tuz, V. Dmitriev, A. B. Evlyukhin, *ACS Appl. Nano Mater.* **2020**, *3*, 11315.
- [25] N. Talebi, S. Guo, P. A. van Aken, *Nanophotonics* **2018**, *7*, 93.
- [26] A. I. Kuznetsov, A. E. Miroshnichenko, M. L. Brongersma, Y. S. Kivshar, B. Luk'yanchuk, *Science* **2016**, *354*, aag2472.
- [27] M. Gupta, R. Singh, *Rev. Phys.* **2020**, *5*, 100040.
- [28] A. Ahmadvand, B. Gerislioglu, R. Ahuja, Y. K. Mishra, *Laser Photon. Rev.* **2020**, *2020*, 1900326.
- [29] S. Lepeshov, Y. Kivshar, *ACS Photonics* **2018**, *5*, 2888.
- [30] O. Tsilipakos, A. C. Tasolamprou, T. Koschny, M. Kafesaki, E. N. Economou, C. M. Soukoulis, *Adv. Opt. Mater.* **2018**, *6*, 1800633.
- [31] A. A. Basharin, V. Chuguevsky, N. Volsky, M. Kafesaki, E. N. Economou, *Phys. Rev. B* **2017**, *95*, 035104.
- [32] S.-D. Liu, Z.-X. Wang, W.-J. Wang, J.-D. Chen, Z.-H. Chen, *Opt. Express* **2017**, *25*, 22375.
- [33] J. Algorri, D. C. Zografopoulos, A. Ferraro, B. García-Cámara, R. Vergaz, R. Beccherelli, J. M. Sánchez-Pena, *Nanomaterials* **2019**, *9*, 30.

- [34] J. Algorri, D. C. Zografopoulos, A. Ferraro, B. García-Cámara, R. Beccherelli, J. M. Sánchez-Pena, *Opt. Express* **2019**, *27*, 6320.
- [35] P. A. Jeong, M. D. Goldflam, S. Campione, J. L. Briscoe, P. P. Vabishchevich, J. Nogan, M. B. Sinclair, T. S. Luk, I. Brener, *ACS Photonics* **2020**, *7*, 1699.
- [36] H. Hasebe, H. Sugimoto, T. Hinamoto, M. Fujii, *Adv. Opt. Mater.* **2020**, *8*, 2001148.
- [37] V. A. Fedotov, A. V. Rogacheva, V. Savinov, D. P. Tsai, N. I. Zheludev, *Sci. Rep.* **2013**, *3*, 2967.
- [38] M. Gupta, V. Savinov, N. Xu, L. Cong, G. Dayal, S. Wang, W. Zhang, N. I. Zheludev, R. Singh, *Adv. Mater.* **2016**, *28*, 8206.
- [39] M. Gupta, R. Singh, *Adv. Opt. Mater.* **2016**, *4*, 2119.
- [40] I. V. Stenishchev, A. A. Basharin, *Sci. Rep.* **2017**, *7*, 9468.
- [41] A. Sayanskiy, M. Danaeifar, P. Kapitanova, A. E. Miroshnichenko, *Adv. Opt. Mater.* **2018**, *6*, 1800302.
- [42] S. Xu, A. Sayanskiy, A. S. Kupriianov, V. R. Tuz, P. Kapitanova, H. B. Sun, W. Han, Y. S. Kivshar, *Adv. Opt. Mater.* **2019**, *7*, 1801166.
- [43] D. C. Zografopoulos, A. Ferraro, J. F. Algorri, P. Martín-Mateos, B. García-Cámara, A. Moreno-Oyervides, V. Krozer, P. Acedo, R. Vergaz, J. M. Sánchez-Pena, R. Beccherelli, *Adv. Opt. Mater.* **2019**, *7*, 1900777.
- [44] Dielectric resonators, E7000 series, <http://www.exxelia.com/uploads/PDF/e7000-v1.pdf> (accessed: February 2021).
- [45] N. Reyes, F. Casado, V. Tapia, C. Jarufe, R. Finger, L. Bronfman, *J. Infrared Millim. Terahertz Waves* **2018**, *39*, 1140.
- [46] C. K. Lee, J. McGhee, C. Tsipogiannis, S. Zhang, D. Cadman, A. Goulas, T. Whittaker, R. Gheisari, D. Engstrom, J. Vardaxoglou, W. Whittow, *Designs* **2019**, *3*, 47.
- [47] D. C. Zografopoulos, J. F. Algorri, A. Ferraro, B. García-Cámara, J. M. Sánchez-Pena, R. Beccherelli, *Sci. Rep.* **2019**, *9*, 7544.
- [48] D. L. Sounas, A. Alù, *Phys. Rev. B* **2018**, *97*, 115431.
- [49] K. V. Baryshnikova, D. A. Smirnova, B. S. Luk'yanchuk, Y. S. Kivshar, *Adv. Opt. Mater.* **2019**, *7*, 1801350.
- [50] A. E. Miroshnichenko, A. B. Evlyukhin, Y. F. Yu, R. M. Bakker, A. Chipouline, A. I. Kuznetsov, B. Luk'yanchuk, B. N. Chichkov, Y. S. Kivshar, *Nat. Commun.* **2015**, *6*, 8069.
- [51] A. K. Ospanova, A. Basharin, A. E. Miroshnichenko, B. Luk'yanchuk, *Opt. Mater. Express* **2021**, *11*, 23.
- [52] V. Savinov, V. A. Fedotov, N. I. Zheludev, *Phys. Rev. B* **2014**, *89*, 205112.
- [53] P. C. Wu, C. Y. Liao, V. Savinov, T. L. Chung, W. T. Chen, Y. W. Huang, P. R. Wu, Y. H. Chen, A.-Q. Liu, N. I. Zheludev, D. P. Tsai, *ACS Nano* **2018**, *12*, 1920.
- [54] X. Chen, Z. Wang, W. Chen, Y. S. Ang, W. Y. Yin, H. Chen, E. P. Li, *IEEE Trans. Antennas Propag.* **2020**, *68*, 5505.
- [55] P. Qin, E. Li, T. Li, H. Ma, Y. Yang, L. K. Ang, H. Chen, *IEEE Trans. Microw. Theory Techn.* **2020**, <https://doi.org/10.1109/tmtt.2020.3027016>.
- [56] O. Luukkonen, C. Simovski, G. Granet, G. Goussetis, D. Lioubtchenko, A. V. Räisänen, S. A. Tretyakov, *IEEE Trans. Antennas Propag.* **2008**, *56*, 1624.
- [57] V. S. Asadchy, M. Albooyeh, S. N. Tcvetkova, A. Díaz-Rubio, Y. Ra'di, S. A. Tretyakov, *Phys. Rev. B* **2016**, *94*, 075142.
- [58] A. Sayanskiy, A. S. Kupriianov, S. Xu, P. Kapitanova, V. Dmitriev, V. V. Khardikov, V. R. Tuz, *Phys. Rev. B* **2019**, *99*, 085306.
- [59] A. S. Kupriianov, Y. Xu, A. Sayanskiy, V. Dmitriev, Y. S. Kivshar, V. R. Tuz, *Phys. Rev. Applied* **2019**, *12*, 014024.
- [60] S. Murai, D. R. Abujetas, G. W. Castellanos, J. A. Sánchez-Gil, F. Zhang, J. G. Rivas, *ACS Photonics* **2020**, *7*, 2204.
- [61] D. R. Abujetas, Á. Barreda, F. Moreno, A. Litman, J.-M. Geffrin, J. A. Sánchez-Gil, *Laser Photon. Rev.* **2020**, *15*, 2000263.
- [62] M. T. Sebastian, R. Uvic, H. Jantunen, *Int. Mater. Rev.* **2015**, *60*, 392.
- [63] Polymethacrylimide foam, Rohacell HF. <https://corporate.evonik.com/en/> (accessed: February 2021).
- [64] Y. Kim, F. Sun, Y. Wang, Y. Qi, J. Lee, Y. Kim, J. Oh, H. Ji, J. Yeo, S. Choi, H. Ryu, H. Noh, T. Kim, *IEEE Wireless Commun.* **2019**, *26*, 2.
- [65] T. Christopoulos, O. Tsilipakos, G. Sinatkas, E. E. Kriezis, *Opt. Express* **2019**, *27*, 14505.
- [66] S. L. Jia, X. Wan, D. Bao, Y. J. Zhao, T. J. Cui, *Laser Photon. Rev.* **2015**, *9*, 545.
- [67] T. Cai, G.-M. Wang, X.-F. Zhang, J.-G. Liang, Y.-Q. Zhuang, D. Liu, H.-X. Xu, *IEEE Trans. Antennas Propag.* **2015**, *63*, 5629.
- [68] D. J. Bisharat, S. Liao, Q. Xue, *IEEE Trans. Antennas Propag.* **2016**, *64*, 33.
- [69] M. A. Abdelaal, A. A. Kishk, *IEEE Trans. Microw. Theory Techn.* **2019**, *67*, 3361.

ADVANCED OPTICAL MATERIALS

Supporting Information

for *Adv. Optical Mater.*, DOI: 10.1002/adom.202002143

All-Dielectric Toroidal Metasurfaces for Angular-
Dependent Resonant Polarization Beam Splitting

Dimitrios C. Zografopoulos, José Francisco Algorri,
Walter Fuscaldo, José Miguel López-Higuera, Ricardo
Vergaz, José Manuel Sánchez-Pena, Ion-Anastasios
Karlolos, Romeo Beccherelli, Vassilios E. Tsioukas,
Traianos V. Yioultsis, and Emmanouil E. Kriezis*

Supporting Information:

All-dielectric toroidal metasurfaces for angular-dependent resonant polarization beam splitting

D. C. Zografopoulos,^{*,†} J. F. Algorri,[‡] W. Fuscaldo,[†] J. M. López-Higuera,^{‡,¶,§} R.
Vergaz,^{||} J. M. Sánchez-Pena,^{||} I.-A. Karolos,[⊥] R. Beccherelli,[†] V. E. Tsioukas,[⊥]
T. V. Yioultsis,[#] and E. E. Kriezis[#]

[†]*Consiglio Nazionale delle Ricerche, Istituto per la Microelettronica e Microsistemi, Via del
fosso del cavaliere 100, Rome 00133, Italy*

[‡]*Photonics Engineering Group, University of Cantabria, Santander 39005, Spain*

[¶]*CIBER-bbn, Instituto de Salud Carlos III, Madrid 28029, Spain*

[§]*Instituto de Investigación Sanitaria Valdecilla (IDIVAL), Santander 39011, Spain*

^{||}*Department of Electronic Technology, Carlos III University of Madrid, Madrid 28911,
Spain*

[⊥]*School of Rural and Surveying Engineering, Aristotle University of Thessaloniki,
Thessaloniki 54124, Greece*

[#]*School of Electrical and Computer Engineering, Aristotle University of Thessaloniki,
Thessaloniki 54124, Greece*

E-mail: dimitrios.zografopoulos@artov.imm.cnr.it

S1. Fabrication of the substrates with 3D-printing

The substrates of both metasurfaces investigated are made of PLA (polylactic acid) material.^{S1,S2} They were 3D-printed in a Prusa i3 MK3 printer using FFF (Fused Filament Fabrication) printing technology, also referred to as FDM (Fused Deposition Modelling). The g-code file was created with the accompanied Prusa Slic3r software application. Resolution for head movement in the x-y plane was set to fine (150 μm), corresponding to the highest possible printing quality, and the filling factor (infill percentage) was set to 100%. The printed model has a solid 1 mm base, on top of which develops the openings lattice that firmly holds the dielectric resonators. Total printing time is less than 3 hours and an almost finished substrate sample is shown in Fig. S1 during the printing process. Samples were inspected to assess deviations from the nominal dimensions, which were found to be below 0.5%.

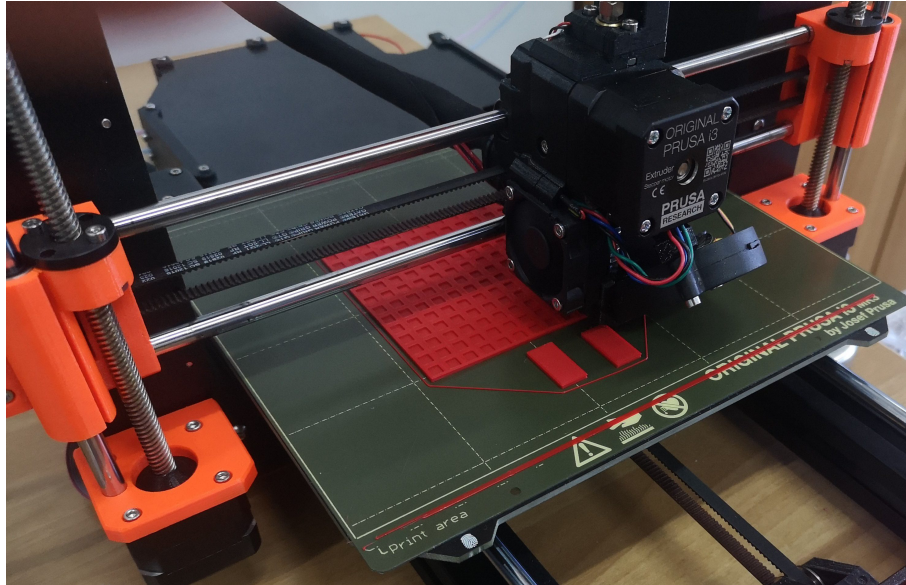


Figure S1: Metasurface substrate printed with PLA in a Prusa i3 MK3 printer. In addition to the metasurface substrate, two solid PLA plates are concurrently printed, that will be subsequently used for characterizing the PLA permittivity, as will be outlined in Section S2.

S2. Waveguide X-band measurements of the PLA permittivity

The substrate material (polylactic acid, PLA) was experimentally characterized in the microwave X-band in order to determine the real and imaginary parts of the relative permittivity. For this purpose, PLA samples exactly matching the cross section of a WR-90 waveguide ($22.86 \times 10.16 \text{ mm}^2$) were prepared and placed in an empty section, as shown in Fig. S2(a). The waveguide holding the sample was attached to the measurement ports marked as Ports 1 and 2 in Fig. S2(b), which are connected to the vector network analyzer (ANRITSU MS 37397D). Additional waveguide sections are seen in Fig. S2(b) between the coaxial cables and the measurement ports to provide further suppression of higher order modes, if excited, and calibration is performed with reference to Ports 1 and 2.

The sample under test is assumed to be nonmagnetic ($\mu_r = 1$) with complex relative permittivity $\varepsilon_r = \varepsilon_r' + j\varepsilon_r'' = \varepsilon_r'(1 - j \tan \delta)$. A filled waveguide section of length d is represented by the ABCD matrix^{S3}

$$\begin{bmatrix} A & B \\ C & D \end{bmatrix} = \begin{bmatrix} \cos(\beta d) & jZ_{\text{WG}} \sin(\beta d) \\ j \sin(\beta d)/Z_{\text{WG}} & \cos(\beta d) \end{bmatrix}, \quad (\text{S1})$$

$$\beta = \sqrt{\omega^2 \varepsilon_0 \varepsilon_r \mu_0 \mu_r - (\pi/a)^2}, \quad (\text{S2})$$

$$Z_{\text{WG}} = \omega \mu_0 \mu_r / \beta, \quad (\text{S3})$$

and directly allows to determine the transmission coefficient between the sample planes as

$$T \equiv S_{21}^{(s)} = \frac{2}{A + B/Z_0 + CZ_0 + D} = \frac{2}{2 \cos(\beta d) + j (Z_{\text{WG}} Z_0^{-1} + Z_{\text{WG}}^{-1} Z_0) \sin(\beta d)}. \quad (\text{S4})$$

In Eq. (S4) Z_0 is the wave impedance of the air-filled waveguide. The VNA records the scattering parameters at the measurement Ports 1 and 2 and thus the measured S_{21} should

be translated to the sample planes. This simply accounts for the phase correction

$$S_{21}^{(s)} = S_{21} \exp[j\beta_0(d_{\text{WG}} - d)], \quad (\text{S5})$$

with β_0 being the phase constant of the air-filled waveguide and d_{WG} the length of the accommodating waveguide. Combining Eq. (S4) with Eq. (S5) develops a single equation involving the complex unknown value $\varepsilon_r = \varepsilon'_r + j\varepsilon''_r$,

$$F(\varepsilon'_r, \varepsilon''_r) = 2 - [2 \cos(\beta d) + j (Z_{\text{WG}} Z_0^{-1} + Z_{\text{WG}}^{-1} Z_0) \sin(\beta d)] S_{21} \exp[j\beta_0(d_{\text{WG}} - d)] = 0. \quad (\text{S6})$$

Eq. (S6) is cast as a nonlinear system of two equations involving the unknown real quantities $(\varepsilon'_r, \varepsilon''_r)$,

$$\text{Re} \{F(\varepsilon'_r, \varepsilon''_r)\} = 0, \quad (\text{S7})$$

$$\text{Im} \{F(\varepsilon'_r, \varepsilon''_r)\} = 0, \quad (\text{S8})$$

which are numerically solved, concluding the ε_r inversion. The above inversion procedure is solely based on the measurement of the transmission coefficient (S_{21}).

Measured PLA samples were produced by 3D-printing with a thickness of 5 mm or 10 mm, leading to almost identical results. Due to the low losses exhibited by the material, it is important to characterize samples having a thickness of at least few mm. Measurements were taken with the sample placed at 10 different sliding positions along the waveguide, to average out small errors (for instance in sample orientation or due to waveguide imperfections). VNA calibration was Through-Reflect-Match (TRM). All measurement points appear in red dots, with Fig. S2(c) showing the real part of relative permittivity (ε'_r) and Fig. S2(d) the imaginary part (ε''_r). Thick black curves correspond to the average value over the different sample positions. The average values in the frequency window examined are $\varepsilon'_r = 2.685$ and $\varepsilon''_r = -0.0268$ ($\tan \delta = 0.01$), well aligned to PLA permittivity values reported in

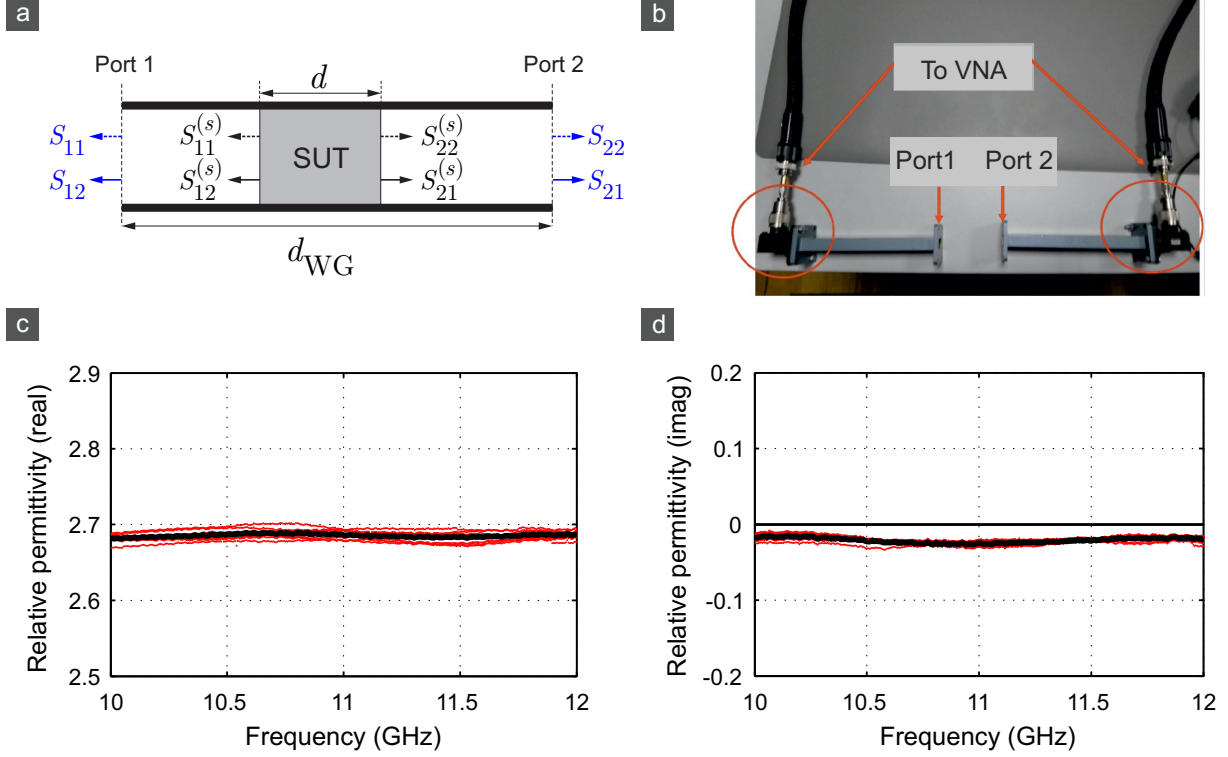


Figure S2: (a) Sample placement for waveguide measurements in transmission. (b) Photo of the setup showing the measurement ports, which are attached to a straight waveguide section that accommodates the sample under test (SUT), as schematically illustrated in (a). Real (c) and imaginary (d) relative permittivity of the measured PLA sample. Red dots correspond to measurements taken at 10 different sample positions along the waveguide, with the black solid curves being the averages over the different positions. Nominal PLA sample thickness was 10 mm, with the actual value after 3D-printing measured at 9.96 mm.

literature.^{S1,S2} Finally, given the minimal levels of dispersion exhibited in the X-band, we feel confident that the above measured values can be appointed also to the frequency range 18-24 GHz that is of interest to the metasurfaces discussed in this work.

S3. Multipole decomposition in Cartesian coordinates

The scattering properties of the resonators as defined in Fig. 2, are investigated by the Cartesian multipole decomposition method. First, the electric field $\mathbf{E}(\mathbf{r})$ inside the cuboid is calculated by employing the scattered-field formulation in the finite-element method imple-

mented in the commercial software Comsol Multiphysics. Then, the multipole decomposition is used in order to identify the individual contributions of the dipole and quadrupole electric, magnetic, and toroidal moments to the total scattering cross-section of the resonators.^{S4-S9}

In particular, the induced polarization current density $\mathbf{J}(\mathbf{r})$ in the resonators, for the $e^{j\omega t}$ convention for the harmonic electromagnetic fields, is calculated as

$$\mathbf{J}(\mathbf{r}) = j\omega (\varepsilon_p - \varepsilon_b) \mathbf{E}(\mathbf{r}), \quad (\text{S9})$$

where ω is the angular frequency and $\varepsilon_p = \varepsilon_{r,p}\varepsilon_0$ and $\varepsilon_b = \varepsilon_{r,b}\varepsilon_0$ are the permittivities of the resonator and surrounding medium, respectively, ε_0 being the vacuum permittivity. In the cases here studied, the surrounding medium is air $\varepsilon_{r,b} = 1$.

The dipole moments for the Cartesian electric, magnetic, and toroidal modes are calculated as

$$\mathbf{p} = \frac{1}{j\omega} \int_V \mathbf{J}(\mathbf{r}) d\mathbf{r} \quad (\text{S10})$$

$$\mathbf{m} = \frac{1}{2v_b} \int_V [\mathbf{r} \times \mathbf{J}(\mathbf{r})] d\mathbf{r} \quad (\text{S11})$$

$$\mathbf{t} = \frac{1}{10v_b} \int_V [(\mathbf{r} \cdot \mathbf{J}(\mathbf{r})) \mathbf{r} - 2r^2 \mathbf{J}(\mathbf{r})] d\mathbf{r}, \quad (\text{S12})$$

where $v_b = c_0/\sqrt{\varepsilon_{r,b}}$ is the speed of light in the surrounding medium and the integration is performed in the volume of the resonator.

The electric, magnetic, and toroidal quadrupole moments are given by

$$Q_{\alpha\beta}^e = \frac{1}{j\omega} \int_V \left[r_\alpha J_\beta + r_\beta J_\alpha - \frac{2}{3} \delta_{\alpha\beta} (\mathbf{r} \cdot \mathbf{J}(\mathbf{r})) \right] d\mathbf{r} \quad (\text{S13})$$

$$Q_{\alpha\beta}^m = \frac{1}{3v_b} \int_V \left\{ [\mathbf{r} \times \mathbf{J}(\mathbf{r})]_\alpha r_\beta + [\mathbf{r} \times \mathbf{J}(\mathbf{r})]_\beta r_\alpha \right\} d\mathbf{r} \quad (\text{S14})$$

$$Q_{\alpha\beta}^T = \frac{1}{42v_b} \int_V \left[4r_\alpha r_\beta (\mathbf{r} \cdot \mathbf{J}(\mathbf{r})) - 5r^2 (r_\alpha J_\beta + r_\beta J_\alpha) + 2r^2 \delta_{\alpha\beta} (\mathbf{r} \cdot \mathbf{J}(\mathbf{r})) \right] d\mathbf{r}, \quad (\text{S15})$$

where the subscripts $\alpha, \beta = x, y, z$ and δ is the Dirac delta function. In addition, we include

the mean-square radii corrections^{S10} for the magnetic and toroidal dipole, and the magnetic quadrupole,

$$\overline{\mathbf{R}}_m^2 = \frac{1}{20v_b} \int_V [\mathbf{r} \times \mathbf{J}(\mathbf{r})] r^2 d\mathbf{r} \quad (\text{S16})$$

$$\overline{\mathbf{R}}_t^2 = \frac{1}{280v_b} \int_V [3r^2 \mathbf{J}(\mathbf{r}) - 2\mathbf{r}(\mathbf{r} \cdot \mathbf{J}(\mathbf{r}))] r^2 d\mathbf{r} \quad (\text{S17})$$

$$\overline{\mathbf{R}}_{\alpha\beta}^{2,Q_m} = \frac{1}{42v_b} \int_V \left\{ [\mathbf{r} \times \mathbf{J}(\mathbf{r})]_{\alpha} r_{\beta} + [\mathbf{r} \times \mathbf{J}(\mathbf{r})]_{\beta} r_{\alpha} \right\} r^2 d\mathbf{r}. \quad (\text{S18})$$

The mean-square radius corrections for the electric moments are omitted, since they do not contribute to the far-field radiation.^{S4}

The scattering cross-sections corresponding to each moment are given by

$$C_{\text{sca}}^{(\text{ed})} = \frac{k_b^4}{6\pi\varepsilon_b^2} \left| \mathbf{p} - jk_b \left(\mathbf{t} + k_b^2 \overline{\mathbf{R}}_t^2 \right) \right|^2 = \frac{k_b^4}{6\pi\varepsilon_b^2} |\mathbf{p} - jk_b \mathbf{t}^*|^2 \quad (\text{S19})$$

$$C_{\text{sca}}^{(\text{md})} = \frac{k_b^4}{6\pi\varepsilon_b^2} \left| \mathbf{m} - k_b^2 \overline{\mathbf{R}}_m^2 \right|^2 \quad (\text{S20})$$

$$C_{\text{sca}}^{(\text{eq})} = \frac{k_b^6}{80\pi\varepsilon_b^2} \sum_{\alpha\beta} |Q_{\alpha\beta}^e - jk_b Q_{\alpha\beta}^T|^2 \quad (\text{S21})$$

$$C_{\text{sca}}^{(\text{mq})} = \frac{k_b^6}{80\pi\varepsilon_b^2} \sum_{\alpha\beta} \left| Q_{\alpha\beta}^m - k_b^2 \overline{\mathbf{R}}_{\alpha\beta}^{2,Q_m} \right|^2. \quad (\text{S22})$$

assuming unit amplitude for the incident planewave electric field ($\mathbf{E}_{\text{inc}} = e^{-jk_0 z} \mathbf{y}$), where $k_b = 2\pi/\lambda$ is the wavevector and λ the free-space wavelength. The superscripts (ed), (md), (eq), (mq) denote the total electric dipole, magnetic dipole, electric quadrupole, and magnetic quadrupole, respectively. Also, we define \mathbf{t}^* as the corrected toroidal dipole moment.

In the context of identifying and investigating anapole states, it is convenient to define the magnitudes $C_{\text{sca}}^{\text{p}}$ and $C_{\text{sca}}^{\text{t}}$

$$C_{\text{sca}}^{\text{p}} = \frac{k_b^4}{6\pi\varepsilon_b^2} |\mathbf{p}|^2 \quad (\text{S23})$$

$$C_{\text{sca}}^{\text{t}} = \frac{k_b^6}{6\pi\varepsilon_b^2} |\mathbf{t}^*|^2, \quad (\text{S24})$$

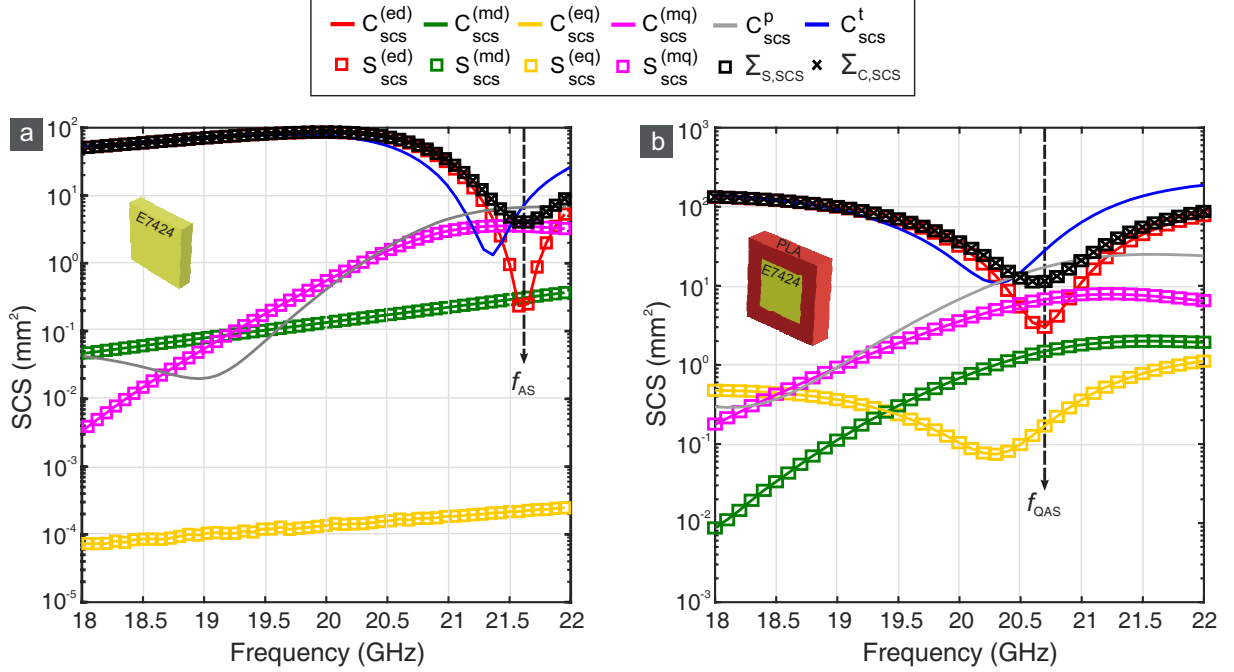


Figure S3: Scattering cross-sections for the dipole and quadrupole moments of a ceramic resonator with $a = b = 4.6$ mm and $h = 1$ mm (a) with and (b) without the PLA frame, calculated by both the Cartesian and the spherical multipole decomposition technique.

which correspond to the cross-sections of the Cartesian electric and toroidal dipoles, respectively. These two dipoles may interfere constructively or destructively and their combined contribution to the total electric dipole scattering cross-section is given in Equation (S19).

Neglecting the contribution of orders higher than the quadrupoles, the total scattering cross-section of the cuboid is approximated as

$$C_{\text{sca}} = C_{\text{sca}}^{(\text{ed})} + C_{\text{sca}}^{(\text{md})} + C_{\text{sca}}^{(\text{eq})} + C_{\text{sca}}^{(\text{mq})}. \quad (\text{S25})$$

Figure S3 shows the SCS for the case of symmetric resonators with and without the PLA frame, as studied in Fig. 2, for the calculated dipole and quadrupole moments. The results are compared with a standard multipole expansion method in spherical coordinates,^{S11} which is integrated in the FEM model, and uses the same polarization currents resulting from the scattered field formulation calculations. Excellent agreement is observed in terms of the SCS for each multipole and their sum. It is remarked that the expansion in spherical functions

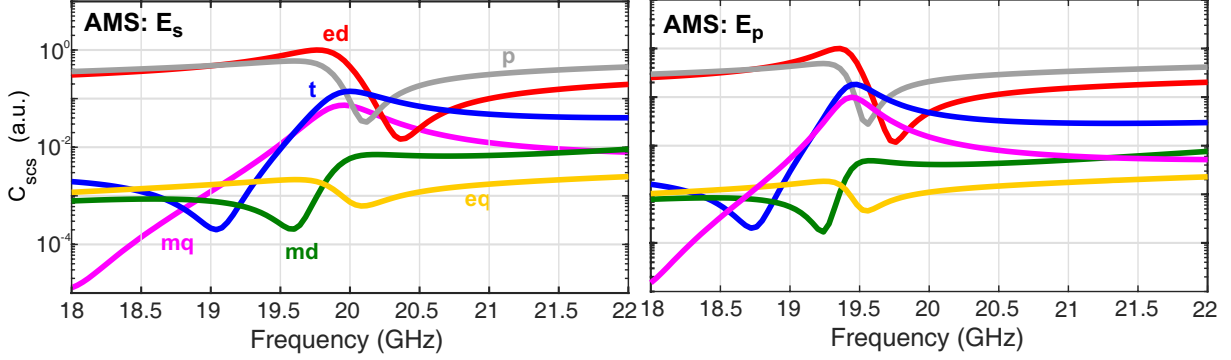


Figure S4: Relative scattering power of the Cartesian electric (p), toroidal (t), total electric (ed), magnetic (md) dipoles, and the electric (eq) and magnetic (mq) quadrupoles for the two polarization cases calculated for the AMS by means of the Cartesian multipole decomposition technique.

does not allow for the individual estimation of the toroidal moments.

By using the above formulation, one can also calculate the relative scattering power of the various multipoles in the case of a periodic metasurface. In that case, the electric field and polarization currents are derived by full-wave FEM simulations using the appropriate periodic boundary conditions at the lateral walls of the unit cell and overall the computational domain. The integration in Eqs. (S10)-(S18) is performed in the volume of the MS unit cell. The resulting absolute values as in Eqs. (S19)-(S24) do not have a physical meaning, such as the SCS in the case of isolated particles, however their relative values can provide indication on the multipolar nature of the resonant MS modes. Figure S4 shows the relative scattering power of the investigated multipoles for the case of the AMS and both polarizations at normal incidence. These results can be directly compared to Fig. 3(b) in the main manuscript, which reports the scattering powers for the SMS case.

S4. Fano fitting of the metasurface spectra

The transmittance spectra of the investigated metasurfaces were calculated by means of full-wave FEM simulations. Subsequently, they were fitted according to the following Fano

Table S4: Fano parameters of the SMS and AMS spectra investigated in Fig. S5.

	C	F	ω_0 (Grad/s)	f_0 (GHz)	γ_n	Q
SMS	0.531	0.782	126.53	20.138 (GHz)	0.01135	44
AMS (s-pol)	0.495	0.859	125.13	19.915 (GHz)	0.01297	38.5
AMS (p-pol)	0.519	0.798	122	19.417 (GHz)	0.00797	62.7

function^{S12}

$$T(\omega_n) = C \frac{(F\gamma_n + \omega_n - 1)^2}{(\omega_n - 1)^2 + \gamma_n^2}, \quad (\text{S26})$$

where C is a scaling parameter, F is the Fano parameter that described the degree of asymmetry, $\omega_n = \omega/\omega_0$ the circular frequency normalized to the resonant frequency ω_0 , and γ_n is the normalized Fano linewidth. The quality factor of the resonance can be calculated as $Q = 1/2\gamma_n$.

Figure S5 provides a comparison between the simulated and Fano-fitted transmittance spectra for the SMS and AMS for both polarizations of a normally impinging planewave. The Fano function in Eq. S26 perfectly captures the spectral profile of the resonances and excellent agreement is observed. From the resulting spectra it can be deduced that the resonance corresponds to the weak coupling regime.^{S13} Indeed, the system supports the strong toroidal resonance, which interacts with the background Fabry-Perot resonance of the slab substrate, which has significantly lower damping. Table S1 summarizes the Fano parameter values for the fitted spectra. In all three cases the Fano asymmetry parameter F is close to unity, which verifies the strongly asymmetric lineshape of the resonances.

S5. Polarization beam splitting at the second working frequency of the asymmetric metasurface

As discussed briefly in Section 4, the AMS allows for PBS operation at two frequencies, which correspond to different working angles of incidence. The low frequency f_l corresponds at the transmittance minimum for the p-polarization, as shown in Fig. 6. Bandstop operation is

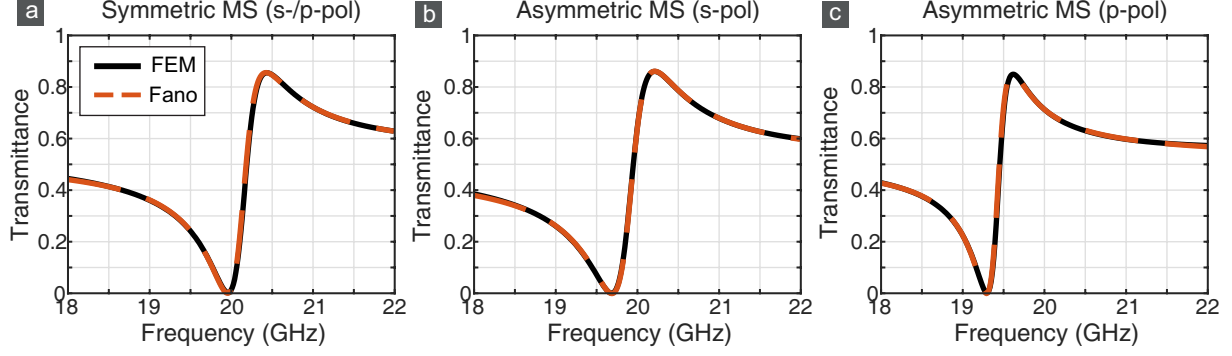


Figure S5: Theoretically calculated and Fano fitted transmittance spectra of the (a) symmetric metasurface, (b) asymmetric metasurface for s-polarized impinging wave and (c) asymmetric metasurface for p-polarized impinging waves. The theoretically calculated spectra correspond to those studied in Fig. 3.

achieved at $\theta_1 = 18^\circ$, where the transmittance at f_l is minimized for the s-polarization, as well. At $\theta_2 = 45^\circ$ PBS is achieved as the s-polarized wave is transmitted at approximately 80%.

Figure S6(a) shows the transmittance spectra in linear and logarithmic scale for both polarizations and at the two working angles of incidence. The corresponding extinction ratio and working bandwidth are assessed in Fig. S6(b). This operation mode, namely switching between bandstop and PBS, is qualitatively similar to the functionality achieved by the SMS, albeit with two differences: a) the smaller bandwidth and b) the different, both non-zero, working angles of incidence. In any case, it is important to note that the AMS provides two operation modes, as discussed in Section 4. Therefore, the AMS could provide double functionality with the same component, should the bandwidth and working angles are compatible with the envisaged application.

S6. Excitation of a symmetry-protected bound state in the continuum at oblique incidence

Here, we provide a more detailed investigation of the resonant mode that was observed in the transmittance spectra and the band diagram of the AMS at approximately 21.5 GHz,

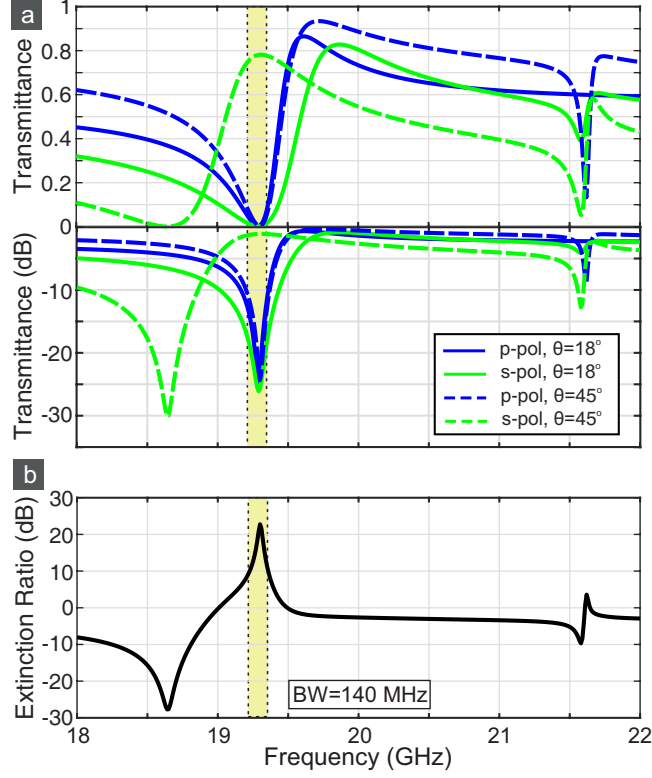


Figure S6: (a) Linear and logarithmic transmittance of the AMS at two angles of incidence $\theta_1 = 18^\circ$ and $\theta_2 = 45^\circ$ for PBS at the second working frequency $f_l = 19.29$ GHz. (b) PBS Extinction ratio. The working bandwidth is marked in yellow shading.

as shown in Fig. 6(a) and (c). It is interesting to note that this mode is not excited at normal incidence, i.e. at the Γ point of the Brillouin zone. This is a feature that provides strong evidence that this particular mode is a symmetry-protected BIC. Such modes coexist in the continuum of radiation modes, yet they remain localized. In their pure form they have infinite lifetime, hence they cannot be excited externally. However, when the symmetry of the structure is broken, their lifetime becomes finite and they can manifest as resonances with a diverging quality factor, as the asymmetry parameter tends to zero.^{S14,S15} One special class of BIC, which are symmetry-protected at the Γ point, is the case of out-of-plane multipolar resonances, the so-called Brewster-like BIC,^{S16} or generally arising due to violation of the uniqueness theorem.^{S17} These BIC are protected at normal incidence but they can be excited by obliquely incident planewaves, where θ plays the role of the symmetry-breaking parameter.

In order to investigate the BIC nature of the observed mode, we calculate the transmit-

tance spectra for the AMS for a varying angle of incidence from $\theta = 0$ to $\theta = 10^\circ$, both including and neglecting all losses of the constituent materials, namely resonators and PLA. In the lossy case, a resonance is excited, as shown in Fig. S7(a), however it can be barely discerned for low θ and overall it is dampened by the absorption losses of the system. On the contrary, in the lossless case an asymmetric Fano resonance is observed, whose quality factor increases as $\theta \rightarrow 0$, whereas the resonance completely disappears at $\theta = 0$, i.e., normal incidence, due to the symmetry-protected nature of the BIC mode.

The quality factor of the resonance for the lossless case is calculated by fitting the spectra to the Fano model as explained in Section S4 and compared with eigenfrequency calculations. The results are presented in Fig. S7(c), where the divergent behaviour of Q is clearly observed. We also investigate the impact of the system losses on the quality factor. In case only the low losses of the ceramic resonators are included, the quality factor is affected for values $Q > 10^4$ and leads to a saturation of $Q \simeq 53000$ at $\theta \rightarrow 0^\circ$. When the losses of PLA are also included, it is evident that the resonance is largely quenched, as also shown in the spectra of Fig. S7(a), and the quality factor remains below $Q < 200$. Nevertheless, the substrate losses can be mitigated to a large extent, as discussed in Section 5. Therefore, this quasi-BIC resonance could achieve high Q -values in a real system, which could be used for highly selective filtering or PBS, although such an analysis lies beyond the scope of this work.

Figure S7(d) shows the electric field profile at the cross-section corresponding at the mid-plane of the resonator along the z -axis and the in-plane electric field vector profile. The field and electric line distribution correspond to an electric quadrupole; in addition, the corresponding profiles at the xz -plane cross-section that splits the resonator in half is also shown.

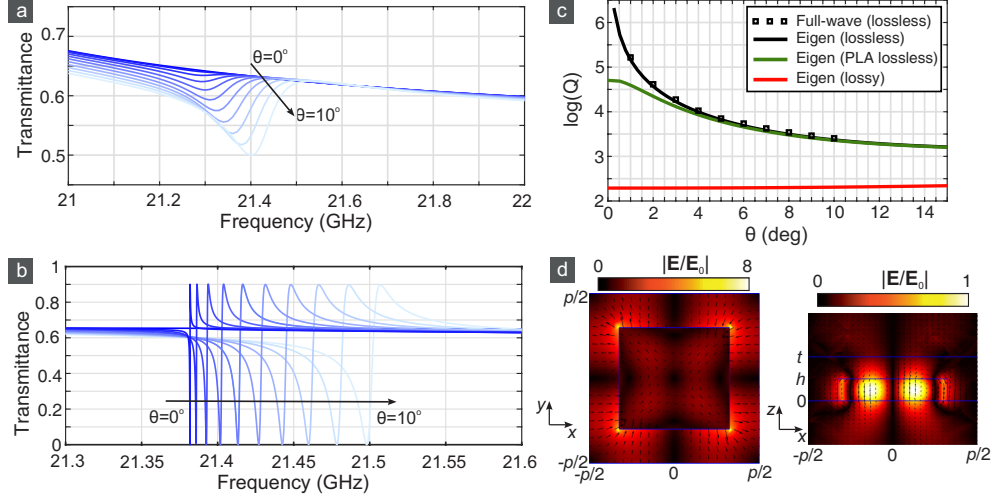


Figure S7: Transmittance spectra of the AMS for an angle of incidence from $\theta = 0^\circ$ to $\theta = 10^\circ$ in steps of 1° (a) including and (b) neglecting the losses of the resonators and the PLA substrate. (c) Quality factor of the investigated BIC resonance for both lossless and loss-including scenarios, extracted from the eigenfrequency problem and the simulated Fano-fitted full-wave spectra. (d) Electric field profile of the BIC calculated at the Γ point of the irreducible Brillouin zone.

References

- [S1] N. Reyes, F. Casado, V. Tapia, C. Jarufe, R. Finger, L. Bronfman, *J. Infrared Millim. Terahertz Waves* **2018**, *39*, 1140.
- [S2] C. K. Lee, J. McGhee, C. Tsiopogiannis, S. Zhang, D. Cadman, A. Goulas, T. Whittaker, R. Gheisari, D. Engstrom, J. Vardaxoglou, W. Whittow, *Designs* **2019**, *3*, 47.
- [S3] Pozar, D. M. *Microwave Engineering*; Wiley, 2004.
- [S4] E. E. Radescu, G. Vaman, *Phys. Rev. E* **2002**, *65*, 046609.
- [S5] Jr. E. Radescu, G. Vaman, *Prog. Electromagn. Res. B* **2012**, *36*, 89.
- [S6] V. Savinov, V. A. Fedotov, N. I. Zheludev, *Phys. Rev. B* **2014**, *89*, 205112.
- [S7] Y. F. Yu, A. Y. Zhu, R. Paniagua-Domínguez, Y. H. Fu, B. Luk'yanchuk, A. I. Kuznetsov, *Laser Photon. Rev.* **2015**, *9*, 412.

- [S8] A. B. Evlyukhin, T. Fischer, C. Reinhardt, B. N. Chichkov, *Phys. Rev. B* **2016**, *94*, 205434.
- [S9] E. A. Gurvitz, K. S. Ladutenko, P. A. Dergachev, A. B. Evlyukhin, A. E. Miroshnichenko, A. S. Shalin, *Laser Photon. Rev.* **2019**, *13*, 1800266.
- [S10] N. A. Nemkov, A. A. Basharin, V. A. Fedotov, *Phys. Rev. A* **2018**, *98*, 023858.
- [S11] P. Grahn, A. Shevchenko, M. Kaivola, *New J. Phys.* **2012**, *14*, 093033.
- [S12] B. Luk'yanchuk, N. I. Zheludev, S. A. Maier, N. J. Halas, P. Nordlander, H. Giessen, C. T. Chong, *Nat. Mater.* **2010**, *9*, 707.
- [S13] M. F. Limonov, M. V. Rybin, A. N. Poddubny, Y. S. Kivshar, *Nature Photon.* **2017**, *11*, 543.
- [S14] A. Sayanskiy, A. S. Kupriianov, S. Xu, P. Kapitanova, V. Dmitriev, V. V. Khardikov, V. R. Tuz, *Phys. Rev. B* **2019**, *99*, 085306.
- [S15] A. S. Kupriianov, Y. Xu, A. Sayanskiy, V. Dmitriev, Y. S. Kivshar, V. R. Tuz, *Phys. Rev. Applied* **2019**, *12*, 014024.
- [S16] D. R. Abujetas, Á. Barreda, F. Moreno, A. Litman, J.-M. Geffrin, J. A. Sánchez-Gil, *Laser Photon. Rev.* **2020**, 2000263.
- [S17] K. Fan, I. V. Shadrivov, W. J. Padilla, *Optica* **2019**, *6*, 169.